



UWL REPOSITORY **repository.uwl.ac.uk**

This is a University of West London scholarly output.

Contact open.research@uwl.ac.uk if you have any queries.

Alternative formats: If you require this document in an alternative format, please contact: open.access@uwl.ac.uk

Copyright: [CC.BY.NC license]

Copyright and moral rights for the publications made accessible in the public portal are retained by the authors and/or other copyright owners and it is a condition of accessing publications that users recognise and abide by the legal requirements associated with these rights.

Take down policy: If you believe that this document breaches copyright, please contact us at open.research@uwl.ac.uk providing details, and we will remove access to the work immediately and investigate your claim.

1 **Modelling and Optimising the Performance of Graphene Oxide-Cu₂SnS₃-Polyaniline**
2 **nanocomposite as an Adsorbent for Mercury Ion Removal**

3 *Sara Enferadi¹, Mohammad Eftekhari², Mohammad Gheibi³, Nikoo Nabizadeh Moghaddam¹,*
4 *Stanislaw Waclawek³, Kouros Behzadian^{4*}*

5 ¹Department of Chemistry, Faculty of Sciences, Ferdowsi University of Mashhad, Mashhad, Iran

6 ²Department of Chemistry, Faculty of Sciences, University of Neyshabur, Neyshabur, Iran

7 ³Institute for Nanomaterials, Advanced Technologies and Innovation, Technical University of Liberec, Studentská
8 1402/2, 461 17 Liberec, Czech Republic

9 ⁴School of Computing and Engineering, University of West London, St Mary's Rd, London, W5 5RF, UK

10 E-mail: kouros.behzadian@uwl.ac.uk

11 **Abstract**

12 Finding a cost-effective, efficient and environmentally friendly technique for removal of
13 mercury ion (Hg²⁺) in water and wastewater can be a challenge task. This paper presents a
14 novel and efficient adsorbent known as the Graphene oxide-Cu₂SnS₃-Polyaniline (GO-CTS-
15 PANI) nanocomposite, which was synthesised and utilised to eliminate mercury ions (Hg²⁺)
16 from water samples. The soft-soft interaction between Hg²⁺ and sulfur atoms besides chelating
17 interaction between -N and Hg²⁺ and also electrostatic interaction are the main mechanisms for
18 Hg²⁺ adsorption onto the GO-CTS-PANI adsorbent. Various characterisation techniques,
19 including Fourier transform infrared spectrophotometry (FT-IR), Field Emission Scanning
20 Electron Microscopy (FESEM), Energy-dispersive X-ray spectroscopy (EDX), Elemental
21 Mapping analysis, and X-ray diffraction analysis (XRD), were employed to analyse the
22 adsorbent. The Box-Behnken method, utilising Design Expert Version 7.0.0, was employed to
23 optimise the crucial factors influencing the adsorption process, such as pH, adsorbent quantity,
24 and contact time. The results indicated that the most efficient adsorption occurred at pH 6.5,

25 with 12 mg of GO-CTS-PANI adsorbent, and a 30-minute contact time, achieving a maximum
26 removal rate of 95% for 50 mg/L Hg^{2+} ions. The study also explored the isotherm and kinetics
27 of the adsorption process, revealing that adsorption took place in sequential layers (Freundlich
28 isotherm) and was followed by a physical interaction between the adsorbent and the adsorbate.
29 The pseudo second-order kinetic equation proved to be a suitable model for interpreting the
30 kinetic data. Furthermore, Response Surface Methodology (RSM) analysis indicated that pH
31 was the most influential parameter in enhancing adsorption efficiency. In addition to traditional
32 models, this study employed artificial intelligence methods, such as the Random Forest
33 algorithm, to enhance the prediction of adsorption process efficiency. The findings
34 demonstrated that the Random Forest algorithm exhibited high accuracy, achieving a
35 correlation coefficient of 0.98. Overall, this research underscores the potential of the GO-CTS-
36 PANI composite for effectively removing Hg^{2+} ions from water resources.

37 **Keywords:** *Adsorption, Artificial Intelligence, Graphene oxide-Cu₂SnS₃-PANI, Mercury ion,*
38 *Response Surface Methodology*

39 **Introduction**

40 In the present era, addressing heavy metal pollution poses a significant challenge to
41 environmental preservation (Briffa et al., 2020). One such hazardous metal is mercury ion
42 (Hg^{2+}), which exhibits toxicity even at low concentrations, leading to detrimental impacts on
43 various bodily systems, including the nervous, digestive, immune, respiratory, and renal
44 systems (Raj and Maiti 2019; Rice et al., 2014). The presence of Hg^{2+} in the environment is
45 primarily attributed to human activities such as gold mining, alloy manufacturing, smelting,
46 electricity and pesticide production, paint manufacturing, and waste incineration (Tchounwou
47 et al., 2003; Mbanga et al., 2019; Streets et al., 2011). It infiltrates water resources through
48 processes like atmospheric deposition, surface runoff, and direct discharge from industries and
49 sewage treatment facilities. Once in water, Hg^{2+} can be converted into methylmercury by

50 bacteria, a highly toxic form of the element. Methylmercury accumulates in the food chain,
51 particularly in aquatic organisms like fish, resulting in biomagnification and posing a health
52 risk to humans when consumed (Global Mercury Assessment 2018; Yu et al., 2016). According
53 to the recent Global Mercury Assessment, approximately 2000-2500 tonnes of mercury are
54 released into the atmosphere, water, and soil each year (Global Mercury Assessment 2018).
55 Consequently, the removal of Hg^{2+} from environmental water samples is of paramount
56 importance.

57 Various techniques, including adsorption (Yu et al., 2016; Santana et al., 2016), membrane
58 filtration (Albatrni et al., 2021; Yan et al., 2021), ion exchange (Han et al., 2020), and
59 coagulation (Vasudevan et al., 2012), have been employed for this purpose. Among these,
60 adsorption is the most commonly used method due to its inherent advantages, including the
61 ease of preparing synthetic and natural adsorbents, relatively low cost, and high removal
62 efficiency (Saadati et al., 2023; Rezazadeh et al., 2022; Wei et al., 2018; Li et al., 2014; Lei et
63 al., 2014).

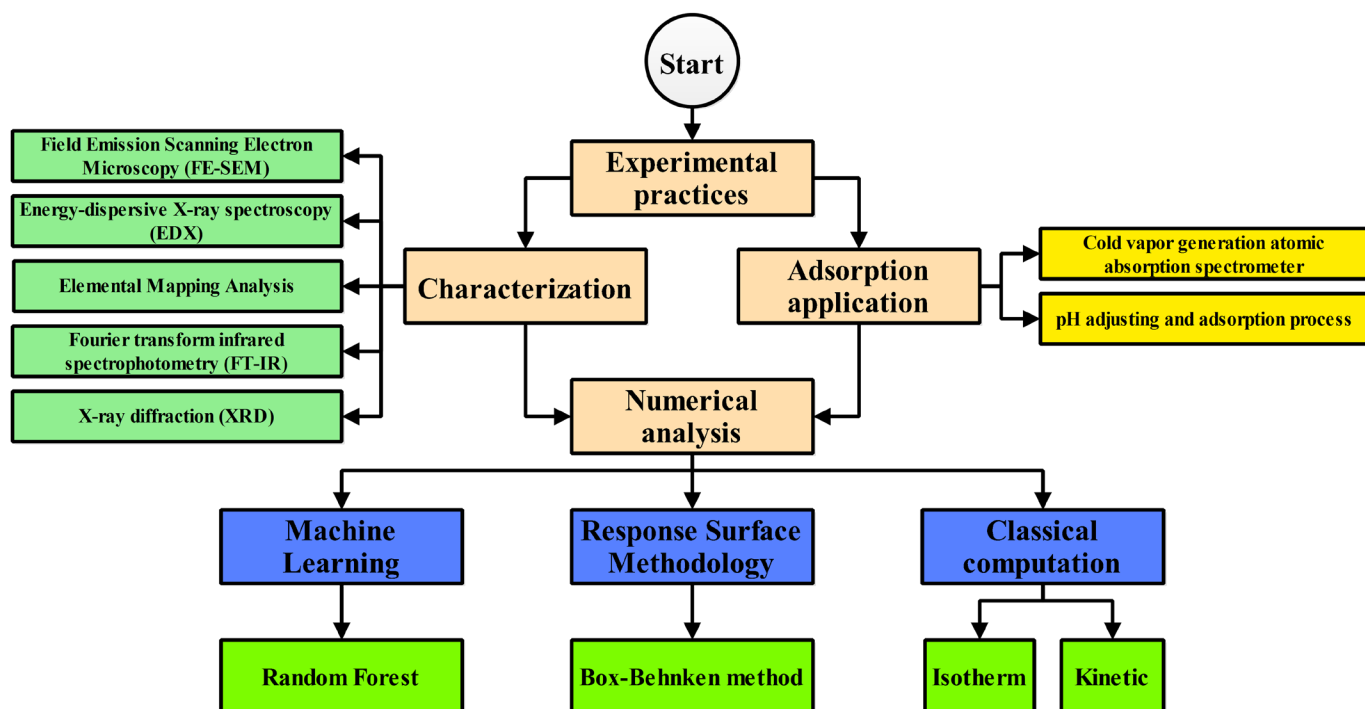
64 Graphene oxide (GO) is an oxidised form of graphene featuring oxygen-based functional
65 groups that render it hydrophilic and readily dispersible in aqueous solutions. Its surface can
66 be chemically or physically modified with various functional groups, making it suitable for a
67 range of applications, including water treatment (Arshad et al., 2019; Amini-Fazl et al., 2021).

68 Ternary Cu_2SnS_3 (CTS) is an environmentally friendly material with optoelectronic properties,
69 well-suited for photoelectrochemical applications (Jathar et al., 2021). It also contains readily
70 available elements, making it a cost-effective material (Berg et al., 2012). Furthermore, the
71 presence of sulfur atoms (soft base) in CTS makes it an effective adsorbent for toxic soft heavy
72 metals like Hg^{2+} (Velempini and Pillay 2019). **Thus, the main purpose of the proposed method**
73 **is to synthesise and characterise of GO-CTS-PANI nanocomposite to be used as an adsorbent**
74 **that would maximise the efficiency of the removal of Hg^{2+} ions from water sample. This can**

75 be achieved by synthesising CTS nanoplates and then its characterisation to modify GO
76 followed by modification with PANI. Since CTS nanoplates have Sulphur atoms in its
77 structure, it could be served as a suitable adsorbent for the removal of Hg^{2+} as a very toxic ion.
78 Hence, this study first aims to synthesise GO nanosheets using the Hummer method and modify
79 them with CTS nanoplates and polyaniline (PANI) to create the GO-CTS-PANI
80 nanocomposite. The synthesised adsorbent undergoes thorough characterisation using various
81 techniques, including Fourier transform infrared spectrophotometry (FT-IR), Field Emission
82 Scanning Electron Microscopy (FESEM), Energy-dispersive X-ray spectroscopy (EDX),
83 Elemental Mapping analysis, and X-ray diffraction analysis (XRD). To determine the optimal
84 conditions for achieving the maximum removal percentage (RP), the Box-Behnken
85 experimental design is employed, and various isotherm and kinetic models are assessed and
86 interpreted. Finally, both the Box-Behnken method and Random Forest algorithms are utilised
87 for optimising and predicting the performance of the adsorption system, respectively.

88 **Methodology**

89 This study is divided to different parts including experimental and numerical efforts which are
 90 demonstrated in **Figure 1**. According to the scheme, it can be found that experimental practices
 91 containing the characterisations and adsorption application process. Likewise, the numerical
 92 parts including classical computations for adsorption mechanism analysis, optimisation by
 93 Response Surface Methodology, and Machine Learning calculations.



94 **Figure 1.** The research roadmap of this study.

95 **Instruments**

96 FE-SEM, EDX, and Elemental Mapping Analysis were conducted using a BRNO-Mira3 LMU
 97 device manufactured by TESCAN in the Czech Republic. FT-IR analysis was performed with
 98 an AVATAR 370 spectrometer from the US, and XRD analysis utilized a D8-Advance Bruker
 99 Cu K α 1 instrument, also from the US. To determine the concentration of Hg²⁺, a cold vapor
 100 generation atomic absorption spectrometer (CV-AAS, Perkin Elmer Analyst 700, USA)
 101 equipped with a Hg hollow cathode lamp emitting at 253.7 nm was employed. pH adjustments
 102 were made with a Metrohm 827 pH-meter from Switzerland, and the separation of the

103 adsorbent from the solution was accomplished using an Andreas Hettich D72 centrifuge
104 instrument from Germany.

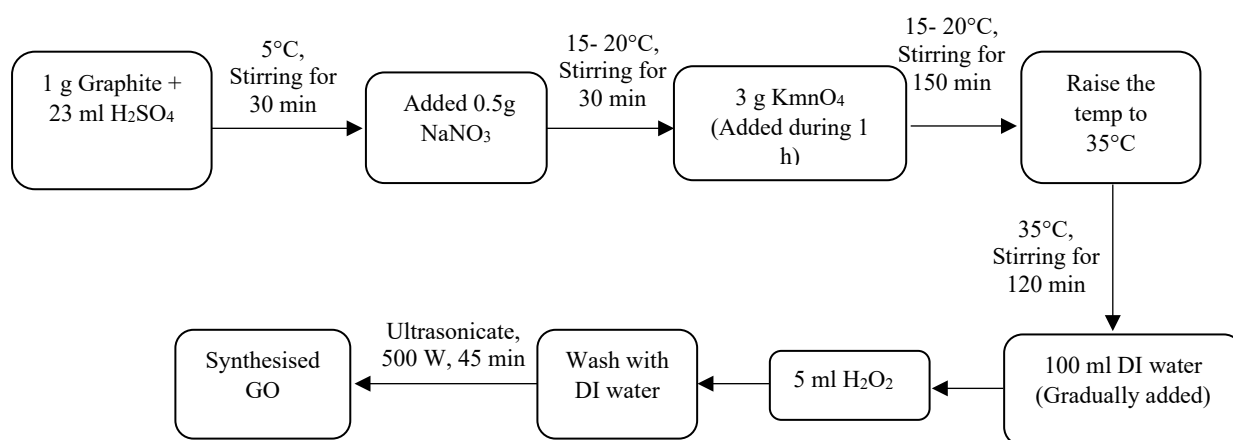
105 Reagents

106 The following reagents and chemicals were used in the experiment: Mercury nitrate
107 monohydrate (Merck, Germany) to prepare a 1000 mg L⁻¹ Hg²⁺ solution, Graphite,
108 Cu(NO₃)₂.3H₂O, SnCl₂.2H₂O, thiourea, aniline, ammonium persulfate, H₂SO₄ (98.0%),
109 KMnO₄ (99.0%), H₂O₂ (30%), sodium borohydride (NaBH₄, 99.0%) and HNO₃ (65.0%). All
110 of these chemicals and reagents were also provided by Merck (Germany).

111 Synthesis of GO-CTS-PANI nano-composite

112 Synthesis of GO and CTS nanoplates

113 GO was synthesised using the Hummers method as described in **Figure 2** (Rezazadeh et al.,
114 2022b). On the other hand, CTS was synthesised according to the following procedure: **0.241**
115 **g Cu(NO₃)₂.3H₂O and 0.114 g SnCl₂.2H₂O were dissolved in 50 ml deionised water. Then**
116 **0.114 g thiourea was added to the mixture which causes to the formation of milky mixture. It**
117 **was then stirred for 30 minutes and autoclaved at 180°C for 8 hours in a 100 mL Teflon-lined**
118 **stainless-steel autoclave. The resulting CTS nanoplates washed with deionised water three**
119 **times and dried overnight at 70 °C (Wang et al., 2017).**



120

121

Figure 2. Synthetic route of GO in this study

122 **Synthesise of GO-CTS nanocomposite**

123 To prepare the GO-CTS nanocomposite; 0.5 g of the synthesised GO in 100 ml deionised water
124 (mixture 1) and 0.15g of CTS nanoplates in 50ml deionised water (mixture 2) were separately
125 ultrasonicated for 45 minutes to obtain uniform mixtures. By addition of mixture 2 into the
126 mixture 1, it was stirred for 6 hours at 400 rpm. The synthesised GO-CTS nanocomposite
127 washed with deionised water three times and dried at 60 °C overnight.

128 **Synthesise of GO-CTS-PANI nanocomposite**

129 In a solution containing 0.5 g of GO-CTS in 100 ml deionised water, 500 µL of aniline (in its
130 monomeric form) was introduced and stirred for a duration of 10 minutes. Following this, 10
131 mL of a 1% ammonium persulfate solution was gradually incorporated into the mixture and
132 stirred for a total of 10 h at 400 rpm. The resulting composite, known as GO-CTS-PANI
133 nanocomposite, underwent multiple washes with deionized water and was subsequently dried
134 overnight at 60 °C.

135 **Removal procedure**

136 In a test solution with an initial Hg^{2+} concentration of 50 mg L⁻¹ at a pH of 6.5, 15 mg of GO-
137 CTS-PANI was introduced, and the blend was agitated for a duration of 45 minutes.
138 Subsequent to centrifugation for 5 min at 5000 rpm, the final concentration of Hg^{2+} at
139 equilibrium was determined using CV-AAS. The removal percentage (RP) and the adsorption
140 capacity (q_e) were computed utilizing Equation (1) and (2), respectively.

141
$$RP = \frac{(C_0 - C_e)}{C_0} \times 100 \quad (1)$$

142
$$q_e = \frac{(C_0 - C_e) \times V}{m} \quad (2)$$

143 where C_e and C_0 = equilibrium and initial concentration of Hg^{2+} in mg per litre, respectively.

144 V = Sample volume in Lit, m = Adsorbent dosage in grams.

145

146 **Optimisation process**

147 In order to enhance the efficiency of the experiment, a Box-Behnken design was utilized
148 through Design Expert Version 7.0.0. The Box-Behnken design belongs to response surface
149 methodology, which constructs a second-order polynomial equation to depict the connection
150 between the influencing factors and the response variable. These influencing factors,
151 encompassing pH, the quantity of adsorbent (M), and contact duration, were modified across
152 three levels, resulting in a total of 15 experimental trials. The mathematical model derived from
153 the Box-Behnken design is represented by Equation 3, as detailed in the work of Eftekhari et
154 al. (2020).

$$155 Y = \beta_0 + \beta_1X_1 + \beta_2X_2 + \beta_3X_3 + \beta_{11}X_1^2 + \beta_{22}X_2^2 + \beta_{33}X_3^2 + \beta_{12}X_1X_2 + \beta_{13}X_1X_3 + \\ 156 \beta_{23}X_2X_3 \quad (3)$$

157 Herein, Y represents the response variable, β_0 is the constant coefficient, β_1 - β_3 are the linear
158 coefficients and β_{11} , β_{22} , and β_{33} are the quadratic coefficients. Moreover, β_{12} , β_{13} , and β_{23}
159 are the interaction coefficients.

160 In the optimisation process, the model performance is examined by desirability functions based
161 on the most important features. The function involves transforming multiple response variables
162 into a single scalar value between 0 and 1, where a value of 1 indicates the optimal condition
163 for all response variables, and a value of 0 indicates the worst condition. The desirability
164 function can be described as the result of multiplying individual desirability functions, with
165 each individual function signifying the degree of desirability for a specific response variable.
166 The allocation of weights for these functions is determined by considering the relative
167 significance of each response variable in relation to the overall performance of the system, as
168 outlined in the work by Eftekhari et al. (2020).

169 **Classical computations**

170 The two-parameter isothermal equations represent mathematical formulas used to describe how
171 adsorption capacity behaves under constant temperature conditions. Meanwhile, the three-
172 parameter isothermal equations share similarities with the two-parameter equations but
173 introduce an additional parameter to better capture the characteristics of the adsorption process
174 (Eftekhari et al., 2020). Initially, the data is analysed using the two-parameter isotherm
175 equations. If both the Langmuir and Freundlich models demonstrate similar performance, then
176 the three-parameter equations are employed to precisely predict the adsorption mechanism
177 (Eftekhari et al., 2020). In this research, both two-parameter models (Dubinin-Radushkevich,
178 Temkin, Langmuir, and Freundlich) and three-parameter models (Toth, Khan, and Sips) are
179 utilized to assess the adsorption mechanism. Furthermore, to evaluate the dynamic behavior of
180 the adsorption process, several kinetic equations are applied (Eftekhari et al., 2020).

181 **Machine Learning calculations**

182 In this current research, the Random Forest (RF) algorithm was employed to predict the
183 removal percentage based on various influential factors, including pH, the quantity of
184 adsorbent, and contact time. The RF algorithm is a machine learning technique that creates
185 numerous decision trees during the training phase and outputs either the mode of the classes
186 (for classification tasks) or the mean prediction (for regression tasks) from the individual trees.
187 In this specific study, the RF algorithm was trained using a dataset comprising known removal
188 percentages and their corresponding influential factors. Additionally, to ensure the accuracy
189 and robustness of the model, the optimal K-fold value was fine-tuned (Eftekhari et al., 2021).
190 The K-fold technique is a method for validating a model, involving the division of the dataset
191 into K equally sized subsets or folds. The model is trained on K-1 folds and tested on the
192 remaining fold, with this process repeated K times. The model's performance is then averaged
193 across the K folds to provide an estimate of its accuracy. In this study, the optimal K value was

194 determined by adjusting the parameter through a grid search approach (Eftekhari et al., 2021).

195 The mathematical representation of the RF algorithm can be found in Equation 4.

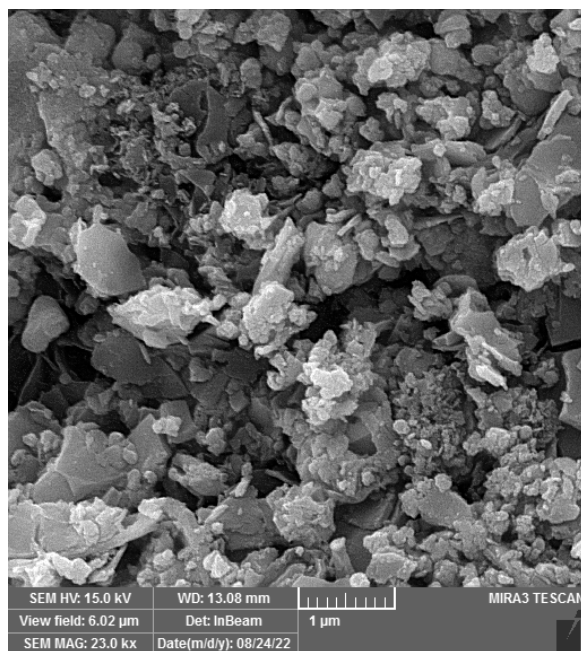
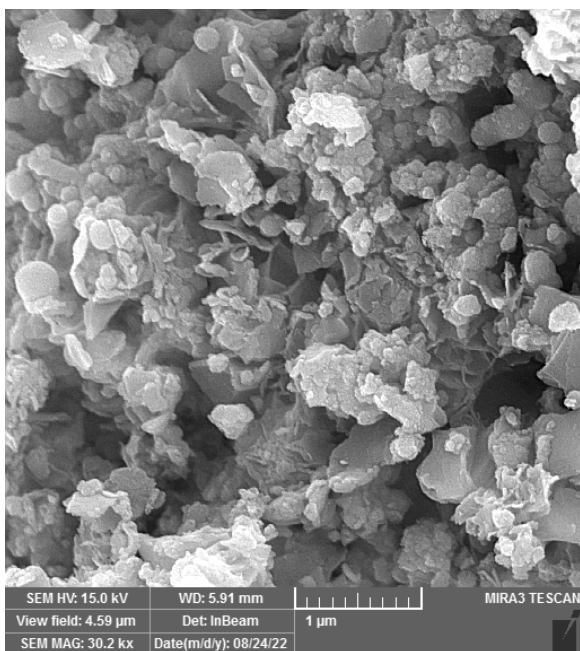
196 Given a training set $T = \{(x_1, y_1), (x_2, y_2), \dots, (x_n, y_n)\}$ (4)

197 In the context of this equation where "xi" represents the influential factors and "yi" stands for
198 the corresponding removal percentage, the RF algorithm generates a diverse set of decision
199 trees denoted as "Ti" by employing bootstrap aggregating, commonly referred to as "bagging,"
200 on the training dataset "T" (Eftekhari et al., 2021). The result produced by the RF algorithm
201 corresponds to the class that emerges as the mode among the classes (for classification tasks)
202 or the mean prediction (for regression tasks) from the individual decision trees. All
203 computational tasks and model training were carried out using WEKA 3.9.

204 **Results and Discussion**

205 **Characterisation of CTS nanoplates and GO-CTS-PANI composite**

206 The CTS nanoplates were synthesised and characterised using XRD, FESEM, and EDX
207 analysis. FESEM images of the synthesised CTS nanoplates are shown in **Figure 3**, while the
208 EDX spectrum presented in **Figure 4** confirms the high purity of CTS nanoplates with peaks
209 corresponding to Cu (0.93 and 8.04 keV), Sn (3.44 keV) and S (2.31 keV). XRD patterns of
210 the synthesised CTS nanoplates are illustrated in **Figure 5**, which shows major diffraction
211 peaks appearing at $2\theta = 28.5^\circ, 32.8^\circ, 47.5^\circ, 56.4^\circ$ and 68.6° . These peaks correspond to (111),
212 (200), (220), (311) and (400) of CTS (JCPDS no. 89-2877), indicating the CTS nanoplates
213 possess a cubic phase (Zaman and Poolla 2020).

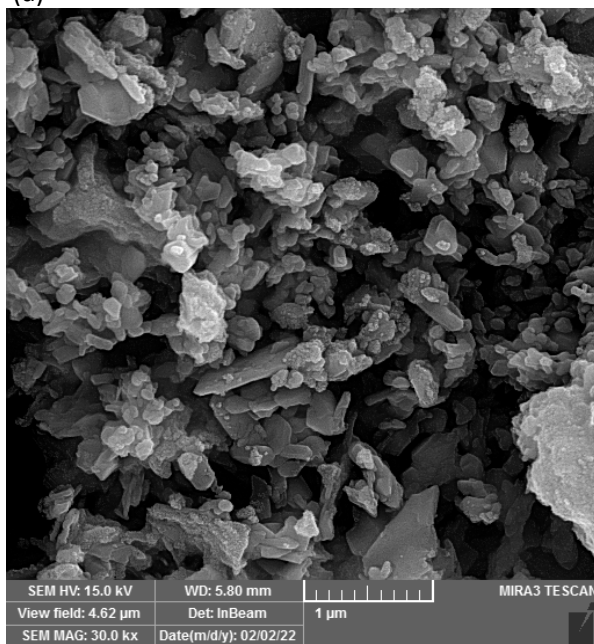


214

215

(a)

(b)



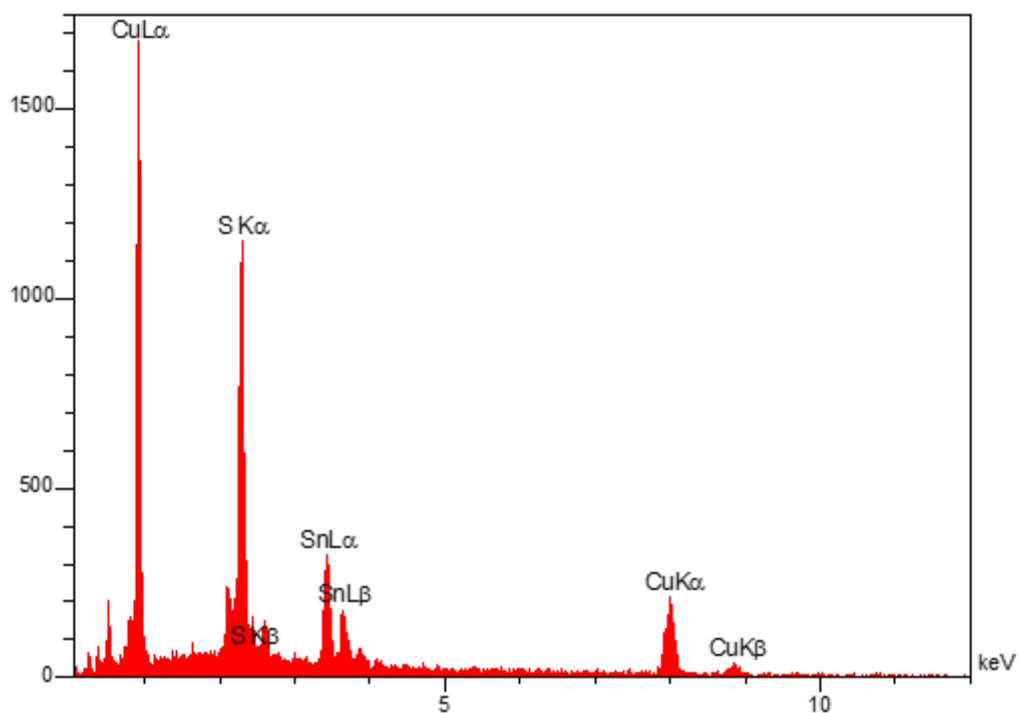
216

217

218

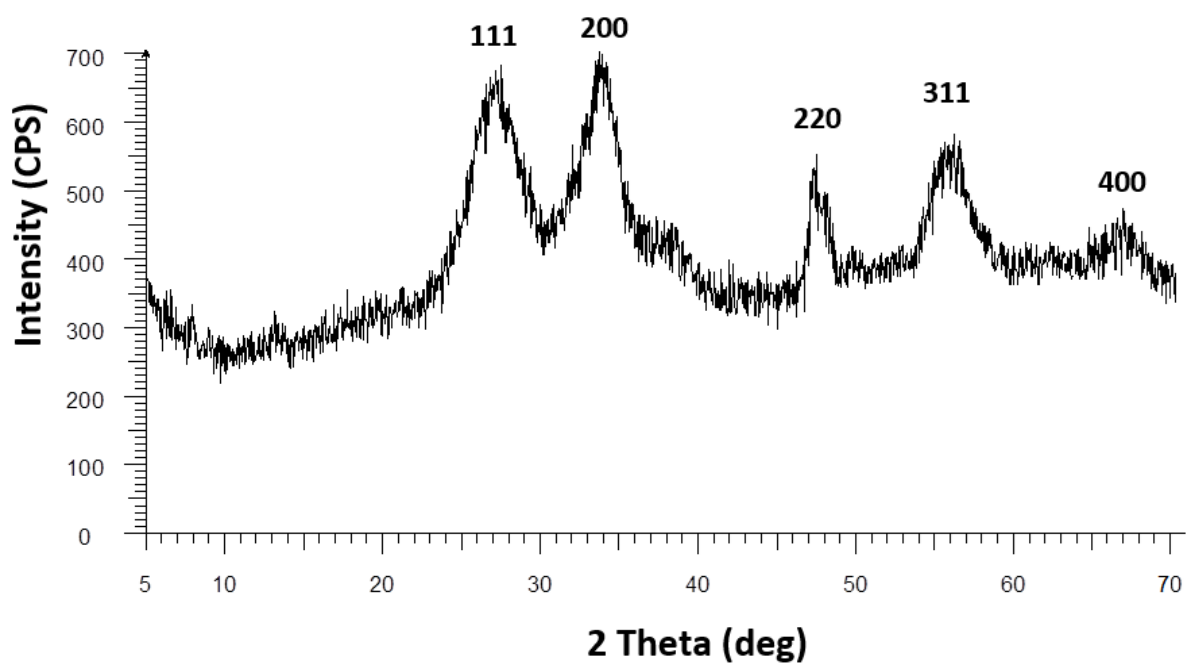
(c)

Figure 3. FESEM images of CTS nanoplates (a-c)



219
220
221

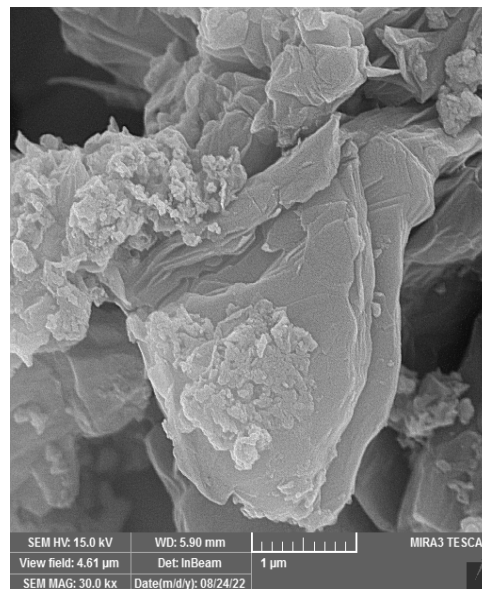
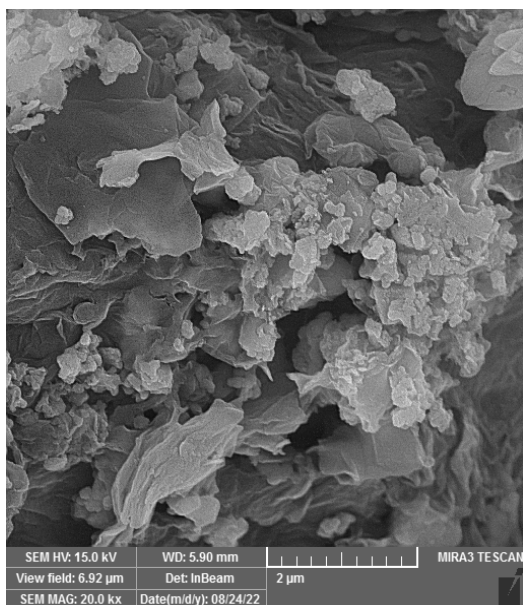
Figure 4. EDX analysis of CTS nanoplates



222
223
224

Figure 5. XRD spectrum of CTS nanoplates

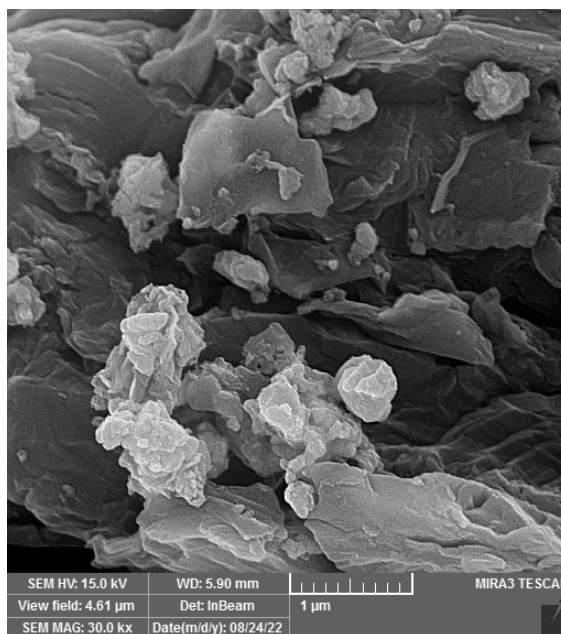
225 **Figure 6** presents FESEM images of GO-CTS-PANI composite, which indicates that GO
226 nanosheets are occupied by CTS nanoplates and PANI. EDX analysis of the composite in
227 **Figure 7** also shows the presence of N and O groups at 0.39 and 0.52 eV, respectively, which
228 are attributed to PANI and GO in the synthesised composite.



230

(a)

(b)



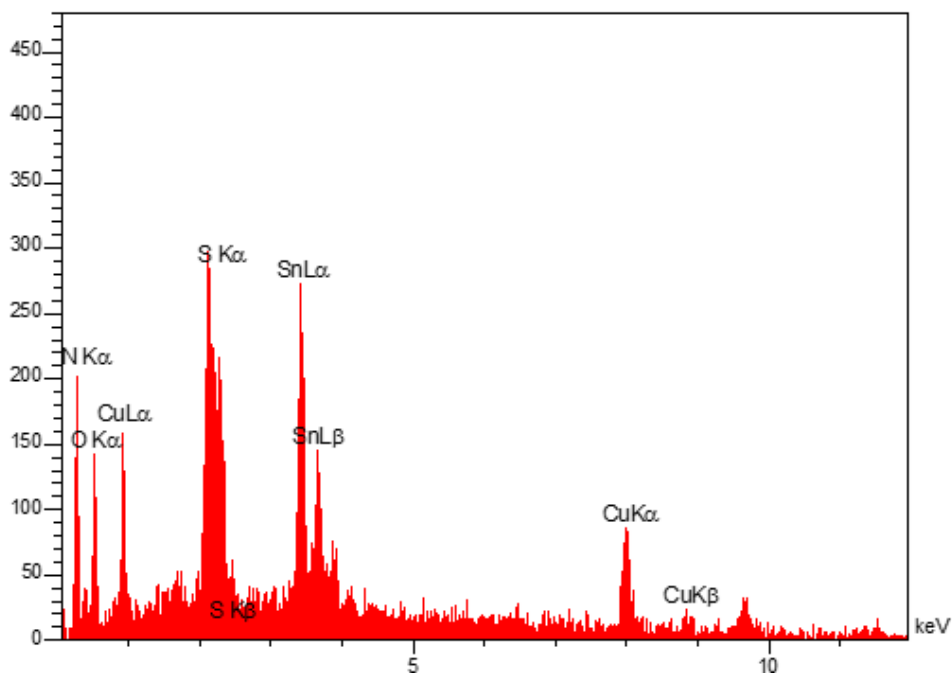
231

232

(c)

233

Figure 6. FESEM images of GO-CTS-PANI nanocomposite



234

235

Figure 7. EDX analysis of GO-CTS-PANI composite

236 The GO-CTS-PANI composite was analysed using XRD in **Figure 8**. The analysis revealed

237 clear appearance of the main peaks of CTS nanoplates in the spectrum. In addition, two peaks

238 of GO at $2\theta = 11.6^\circ$ and 42.5° correspond to (001) and (101), respectively (Shabani-

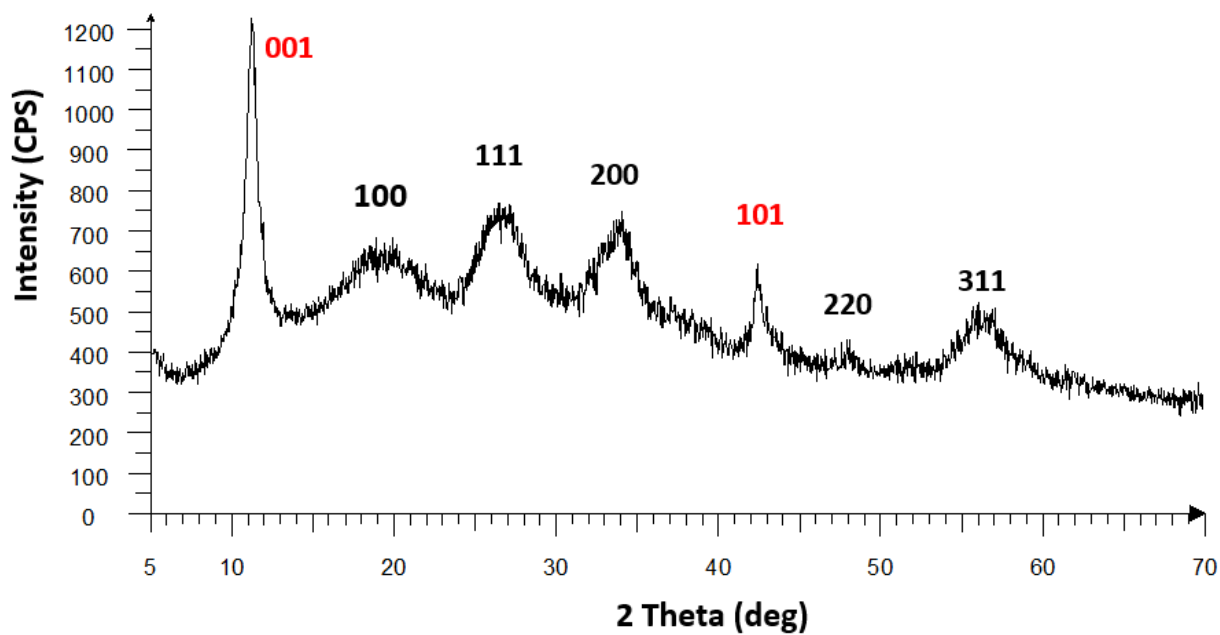
239 Nooshabadi and Zahedi 2019) while a broad peak at $2\theta=20^\circ$ corresponds to (100) and

240 attributed to PANI (Liu et al., 2018).

241

242

243



244

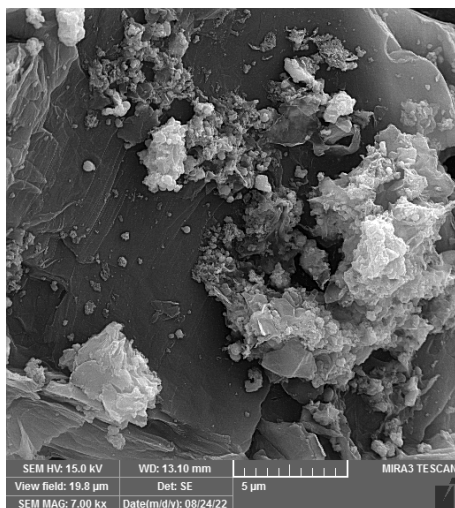
245

Figure 8. XRD spectrum of GO-CTS-PANI nanocomposite

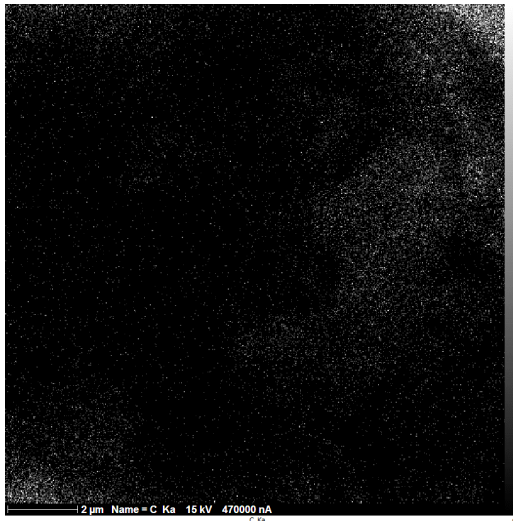
246 MAP analysis was conducted on GO-CTS-PANI nanocomposite, and the results (Figure 9a-

247 e) revealed that C (7a), Cu (7b), N(7c), O(7d), S(7e) and Sn (7f) are the main components of

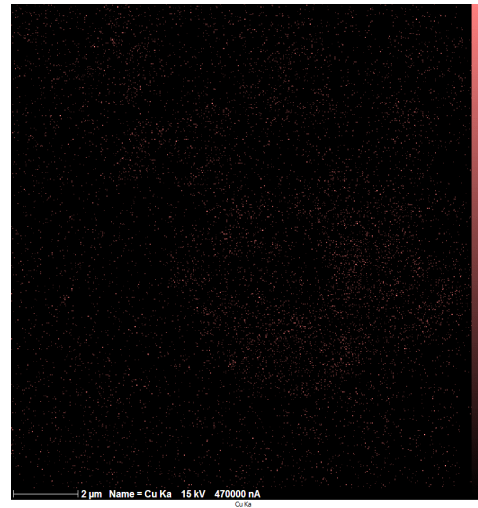
248 the synthesised GO-CTS-PANI nanocomposite.



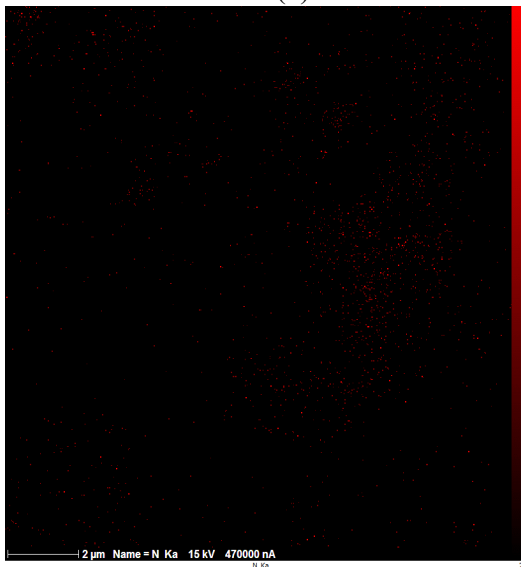
(a)



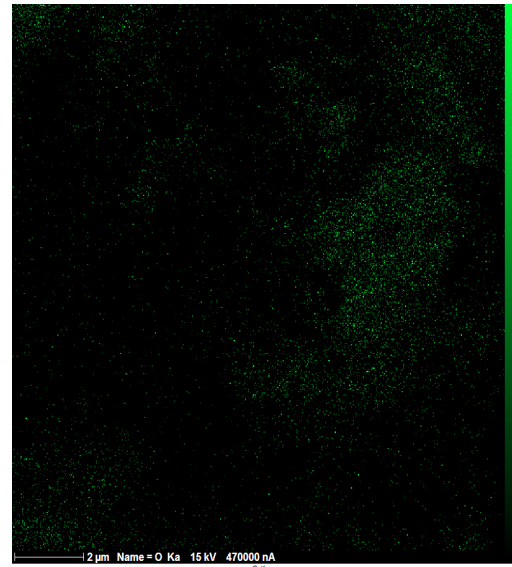
(b)



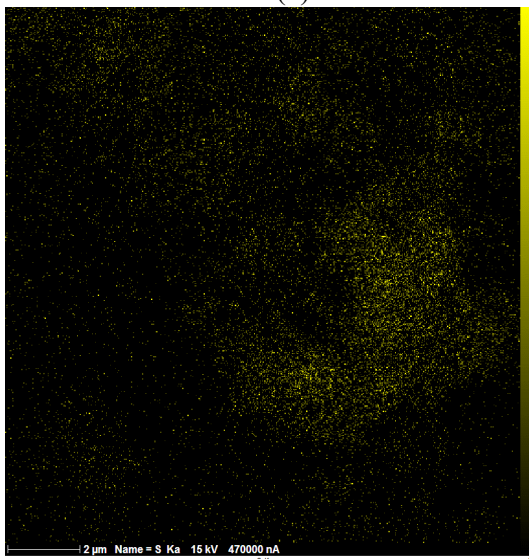
(c)



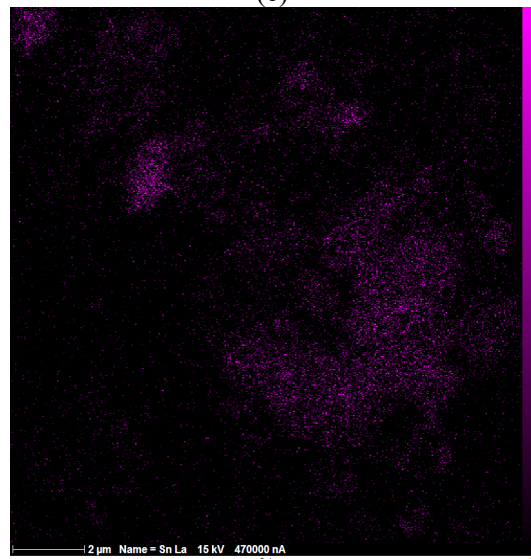
(d)



(e)



(f)



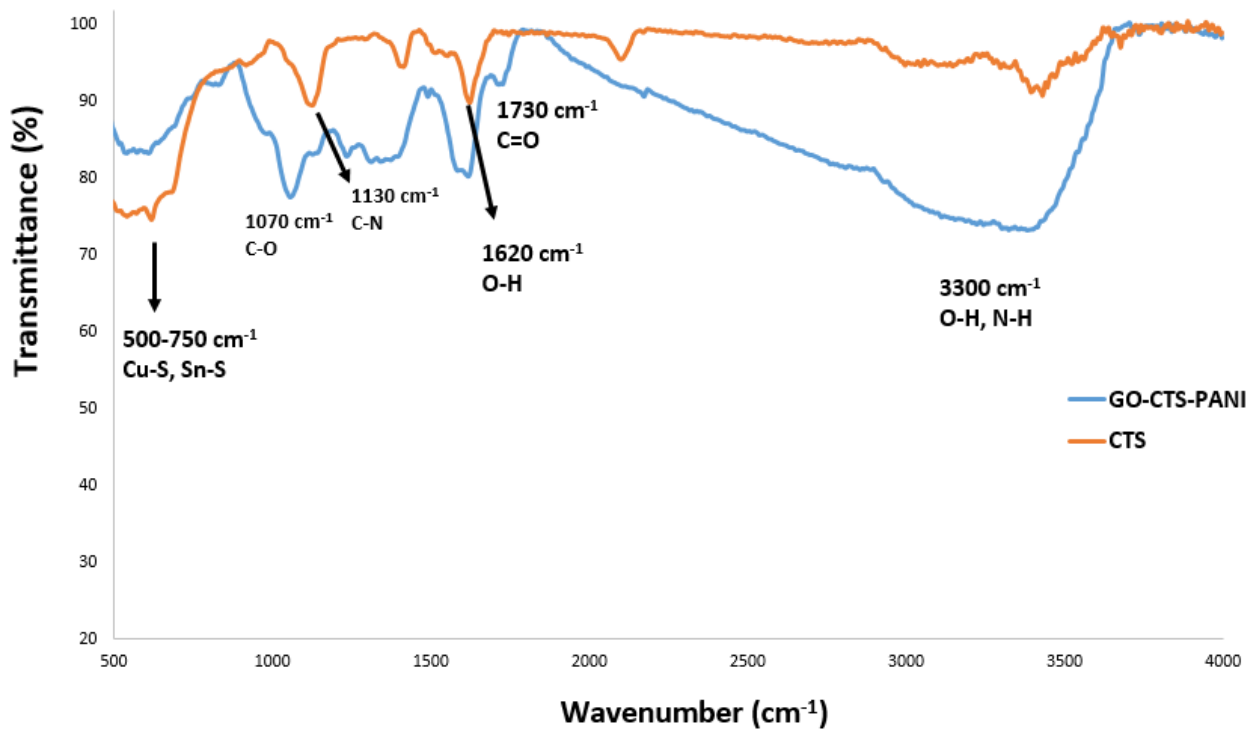
(g)

249 **Figure 9. MAP elemental analysis of GO-CTS-PANI; distribution of mapping zone in SEM image (a) C**

250 **(b), Cu (c), N(d), O(e), S(f) and Sn (g) (a-f images).**

251 Finally, the FT-IR spectra of GO-CTS-PANI composite and CTS nanoplates are presented in
252 **Figure 10**. The CTS spectrum shows a sharp peak at 500-750 cm^{-1} that is related to the
253 vibration of Cu-S, Sn-S bonds. The band at 1630 cm^{-1} is due to the O-H bending of water
254 molecules and a peak appeared at 1130 cm^{-1} could be attributed to the stretching vibration of
255 C-N band of thiourea in the structure of CTS nanoplates. The FT-IR spectrum of GO-CTS-
256 PANI shows the peaks at 3300 cm^{-1} (stretching of N-H, O-H), 1050 cm^{-1} (C-O of hydroxyl
257 group), 1730 cm^{-1} (C=O) and 1650 cm^{-1} (C=C). Moreover, the intense peak of Cu-S and Sn-S
258 (at 500-750 cm^{-1}) in CTS nanoplates is reduced after modification by GO-PANI.

259



260

261 **Figure 10. FT-IR spectrum of the synthesised CTS nanoplates and GO-CTS-PANI**

262

263 **Optimisation of parameters**

264 To optimise effective features including pH, adsorbent amount (M), and contact time, Box-
265 Behnken method was applied using Design Expert Version 7.0.0 for 50 mg L^{-1} Hg^{2+} ion. The

266 range of each parameter in the Design of Experiments (DOE) as well as the statistical analysis
 267 outcomes of experiments are presented in Table 1. The responses obtained from the
 268 experiments are distributed between 36% and 95%. Also, the model follows polynomial and
 269 quadratic equation for fitting effective features as per removal percentage of Hg²⁺. Likewise,
 270 according to Table 1, it can be concluded that there is spread distribution of Hg²⁺ ion
 271 purification from water samples in different conditions of adsorption operation process.
 272 Therefore, finding the optimum condition will be valuable in viewpoints of water treatment
 273 efficiency.

274 **Table 1. The limitations of DOE in this study**

Factor	Name	Units	Type	Low Actual	High Actual	Low Coded	High Coded	Mean	Std. Dev.	
A	pH		Numeric	2	7	-1	1	4.5	1.714986	
B	M	mg	Numeric	5	15	-1	1	10	3.429972	
C	Contact time	min	Numeric	10	50	-1	1	30	13.71989	
Response	Name	Units	Obs	Analysis	Minimum	Maximum	Mean	Std. Dev.	Ratio (max/min)	Model
Y1	RP	%	17	Polynomial	36	95	59.47059	17.9	2.58	Quadratic

275
 276 Table 2 displays various statistical metrics, including Standard Deviation, R-Squared, Adjusted
 277 R-Squared, Predicted R-Squared, and Press, for four distinct models: linear, 2FI, quadratic, and
 278 cubic. As indicated by the information in Table 2, the quadratic model (as described in Equation
 279 3) exhibits superior performance, with an R-Squared value of 0.99 and a Predicted R-Squared
 280 value of 0.94, outperforming the other models. Nevertheless, it's worth noting that the Predicted
 281 R-Squared value can be further enhanced by incorporating machine learning computations.

282

283

Table 2. The curve fitting regression outcomes in different mathematical models.

Source	Std. Dev.	R-Squared	Adjusted R-Squared	Predicted R-Squared	PRESS	
Linear	7.412232	0.869001	0.838771	0.741765587	1407.955	
2FI	8.351559	0.872074	0.795318	0.409168432	3221.353	
Quadratic	2.339108	0.992975	0.983944	0.942684058	312.5	Suggested
Cubic	2.280351	0.996185	0.98474			

285

$$286 \quad \mathbf{RP} = -3.38 - 2.36 * \text{pH} + 5.82 * \text{M} + 1.07 * \text{Contact time} + 0.14 * \text{pH} * \text{M} + 0.015 * \text{pH} * \text{Contact}$$

$$287 \quad \text{time} + 7.5\text{E-}003 * \text{M} * \text{Contact time} + 1.12 * \text{pH}^2 - 0.29 * \text{M}^2 - 0.018 * \text{Contact time}^2$$

288 (3)

289 The Analysis of Variance (ANOVA) results presented in Table 3 demonstrates that the
 290 designed model (Equation 1) is significant with a P-value <0.0001 and the error value in
 291 prediction (lack of fit) is insignificant indicating the validity of the equation. Among the three
 292 parameters (pH, M, and contact time), pH has the smallest P-value (<0.0001) and largest F-
 293 value (842.19). Between the other two factors, the mass of adsorbent has more importance (P-
 294 value = 0.0039) that the contact time (P-value = 0.0462).

295

Table 3. The results of ANOVA practices in this study

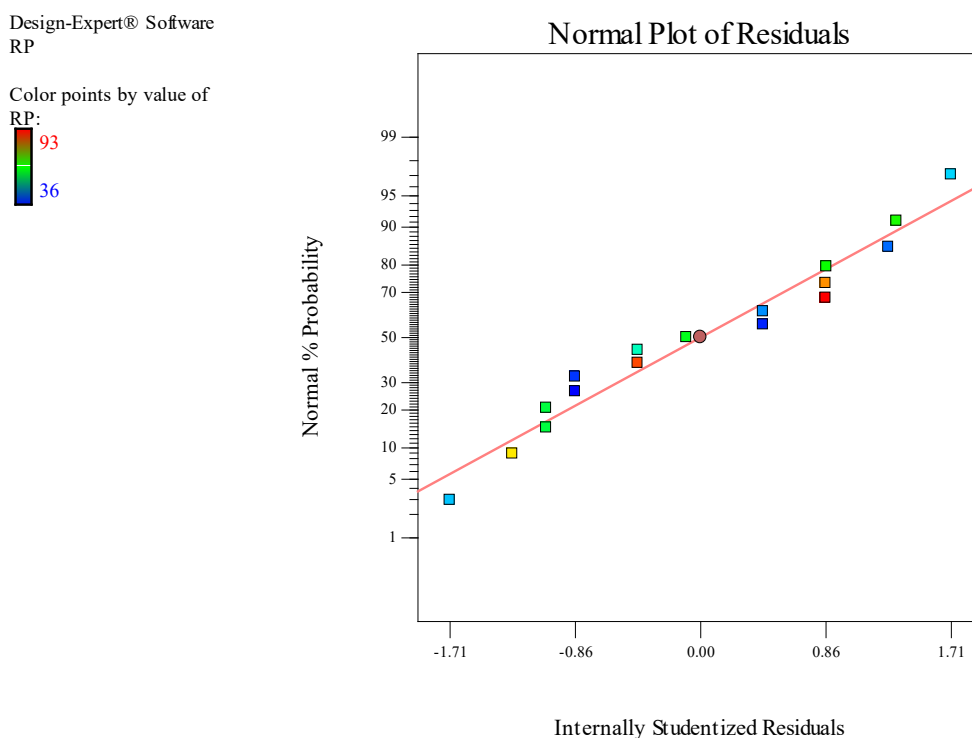
Source	Sum of Squares	Mean Square	F-Value	P-value	
Model	5413.9	601.54	109.9436	< 0.0001	significant
A-pH	4608	4608	842.1932	< 0.0001	
B-M	98	98	17.91123	0.0039	
C-Contact time	32	32	5.848564	0.0462	
AB	12.25	12.25	2.238903	0.1782	
AC	2.25	2.25	0.411227	0.5418	
BC	2.25	2.25	0.411	0.5418	
A^2	207.79	207.79	37.97	0.0005	
B^2	235.26	235.26	42.99	0.0003	
C^2	235.26	235.26	42.99	0.0003	
Residual	38.3	5.47			
Lack of Fit	17.5	5.83	1.12	0.4395	not significant
Pure Error	20.8	5.2			
Cor Total	5452.2				

296 The statistical distribution of results is presented in **Figure 11** (Normal% probability via
297 internally studentised residuals). Based on the results the normality of experimental outputs of
298 the DOE were found to be normal all the data are located within the normal diagram according
299 to the declared scheme. A normally distributed dataset implies that the mean and standard
300 deviation of the data are well-defined, which can aid in the design and optimisation of the
301 system. Additionally, engineers can use this information to make informed decisions about the
302 system, such as setting appropriate tolerances for manufacturing processes or determining the
303 expected variability in system performance. Overall, the normality of the experimental outputs
304 is a useful piece of information for engineers to consider when analysing and designing
305 systems. **Figure 12(a-c)** shows the outcomes of the dual sensitive evaluation of effective
306 experimental factors for adsorption of Hg^{2+} onto GO-CTS-PANI. **Figure 12a** demonstrates the
307 influence of pH and amount of adsorbent on the recovery percentage of Hg^{2+} .

308 The findings suggest that elevating the pH level results in an augmentation of the removal
309 percentage (RP) of Hg^{2+} , reaching its peak effectiveness at around pH 6.5-7. This notable
310 enhancement in RP as pH increases is likely attributed to the deprotonation of functional groups
311 like carboxyl, sulfur, and N-H on the adsorbent, enhancing their interaction with Hg^{2+}
312 (Anirudhan et al., 2015; Gao et al., 2021). Conversely, the lower RP of Hg^{2+} in acidic solutions
313 (pH<5) is linked to the protonation of S-atoms in CTS nanoplates, protonation of hydroxyl
314 groups, incomplete dissociation of carboxylic acid groups (which have pKa values around 5)
315 on GO, and protonation of -NH groups on PANI, leading to electrostatic repulsion between
316 Hg^{2+} ions. Within the pH range of 6–7, Hg^{2+} predominantly exists as $\text{Hg}(\text{OH})_2$ (approximately
317 79%) and HgOH^+ (approximately 10%) (Anirudhan and Shainy 2015). According to the
318 Pearson rule, interactions are more favourable between hard acids and hard bases, and soft
319 acids and soft bases (Santhana Krishna Kumar et al., 2013). Additionally, considering that
320 neutral molecules are softer acids compared to metal cations, the interaction between Hg^{2+}

321 species becomes more favourable at higher pH values. Regarding the influence of the
322 parameter "M" on RP, an increase in "M" enhances the RP of Hg^{2+} because it provides more
323 available active sites for interaction with the analyte. However, a further increase in the "M"
324 parameter eventually diminishes the RP, primarily due to the aggregation of the adsorbent
325 (Eftekhari et al., 2020). **Figures 12b** and **12c** depict the effects of contact time, "M," and pH
326 on the RP of Hg^{2+} , with the results showing that an extended contact time leads to an improved
327 RP of Hg^{2+} . **Figure 13** shows the EDX spectrum of GO-CTS-PANI adsorbent after adsorption
328 of Hg^{2+} that shows a peak of the adsorbed Hg^{2+} at 9.9 keV. The obtained results clearly shows
329 that Hg^{2+} ions effectively adsorbed onto the GO-CTS-PANI adsorbent.

330



331

332

Figure 11. The normal distribution of experimental outcomes in this study

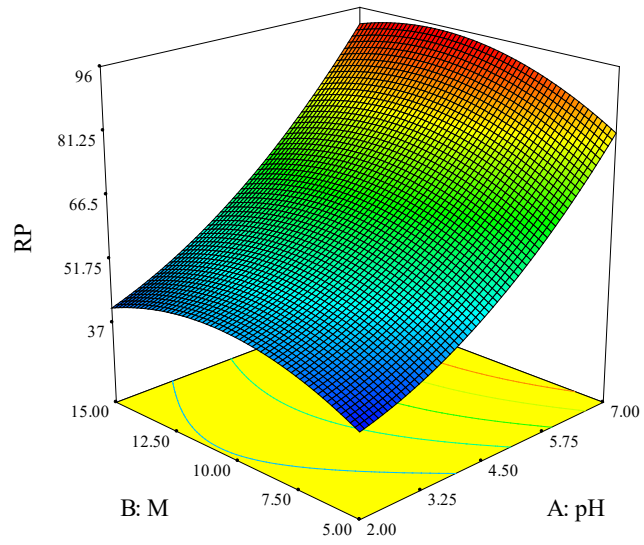
333

Design-Expert® Software



X1 = A: pH
X2 = B: M

Actual Factor
C: Contact time = 30.00



334

335

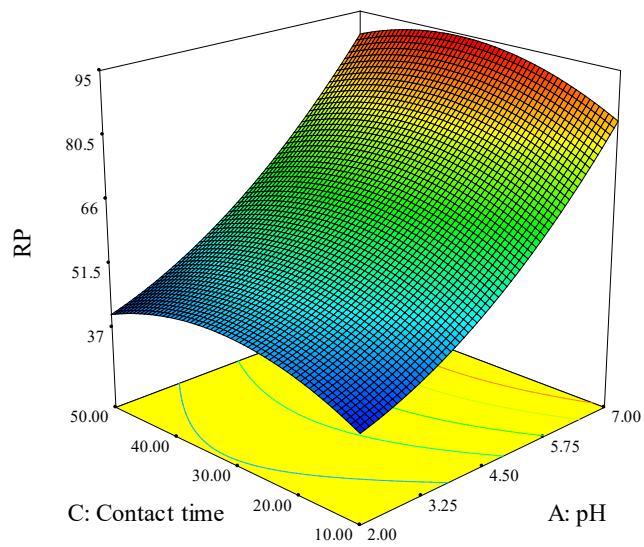
(a)

Design-Expert® Software



X1 = A: pH
X2 = C: Contact time

Actual Factor
B: M = 10.00

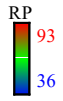


336

337

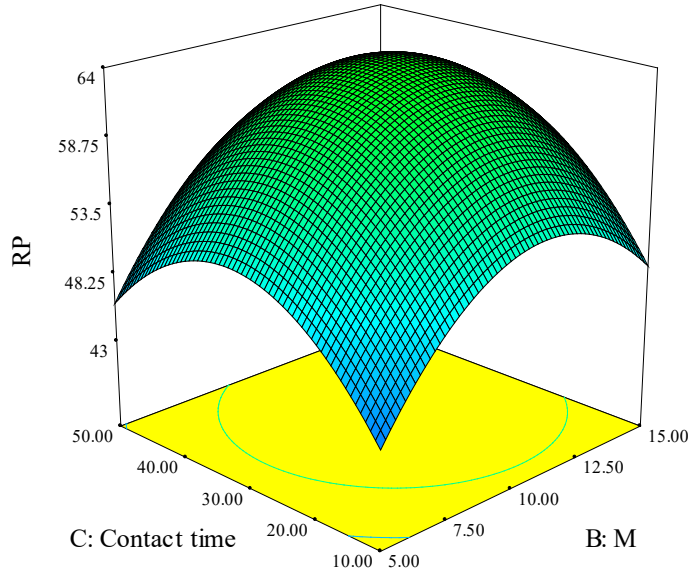
(b)

Design-Expert® Software



X1 = B: M
X2 = C: Contact time

Actual Factor
A: pH = 4.50



(c)

Figure 12. The sensitive analysis of the studied parameters on RP of Hg^{2+} (50 mg L^{-1}) (a-c).

338
339
340
341
342
343

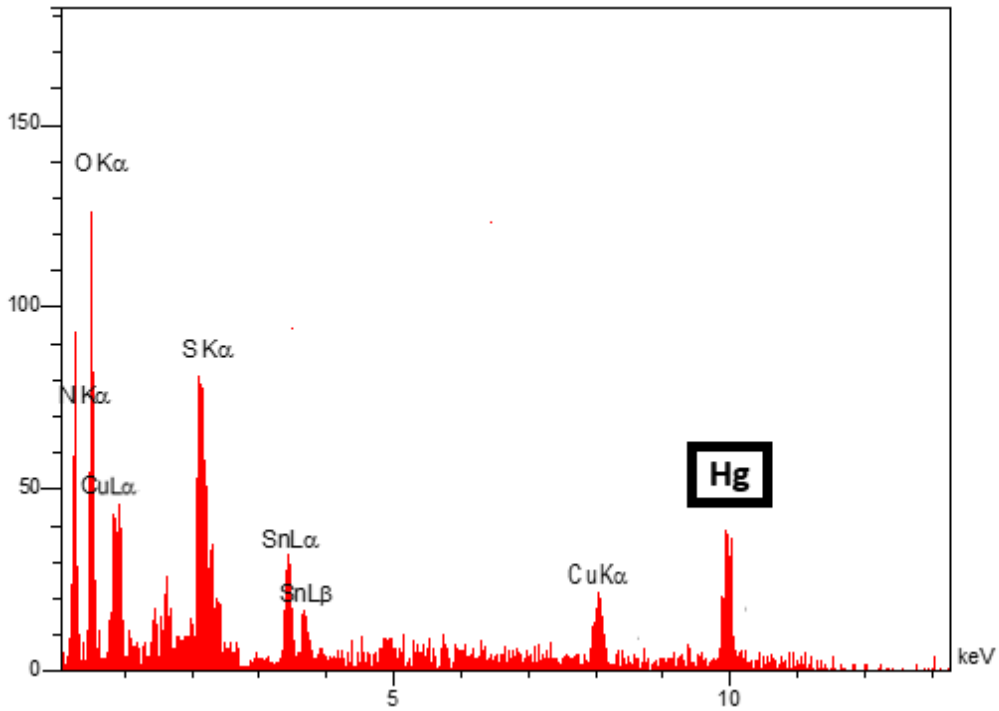


Figure 13. EDX analysis of GO-CTS-PANI after adsorption of Hg^{2+} ions.

344
345

346

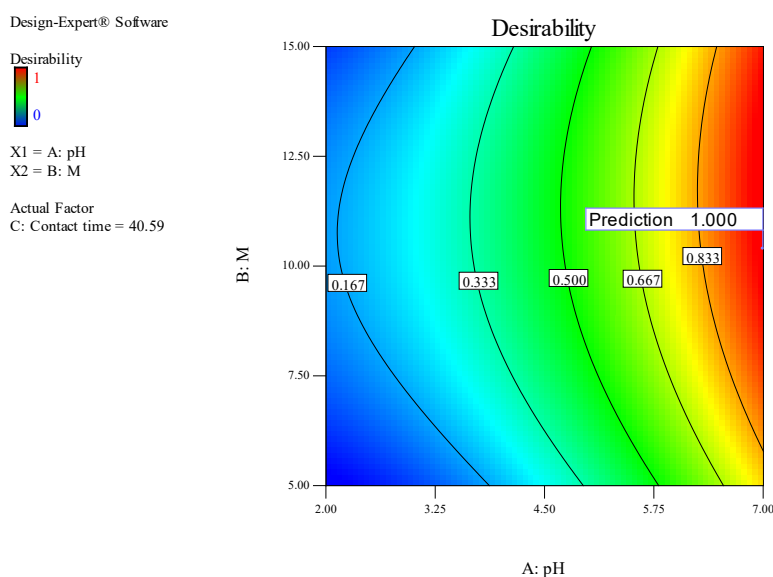
347 After conducting sensitive analysis and mathematical modelling using Box-Behnken model,
 348 the optimal values of the effective factors are computed. The results (Table 4) show that the
 349 maximum performance (removal percentage as RP) for removing Hg^{2+} from water samples
 350 using GO-CTS-PANI is 95%, indicating the best operational efficiency. Therefore, the optimal
 351 performance can be obtained based on optimal features of pH of 6.5, M=12 mg and contact
 352 time of 30 min. These effective features are also depicted in **Figure 14** based on the desirability.
 353 The contours in the figure show that the maximum desirability for predicting the optimal
 354 conditions is achieved with high levels of pH and intermediate values of M.

355

356 **Table 4. The optimal suggestions of effective features based on RP% in this study.**

pH	M (mg)	Contact time (minutes)	RP (%)	Desirability
6.59	10.39	40.59	97	1.000
6.56	10.42	39.18	97.6633	1.000
6.50	12.07	30.38	98.3089	1.000

357



358

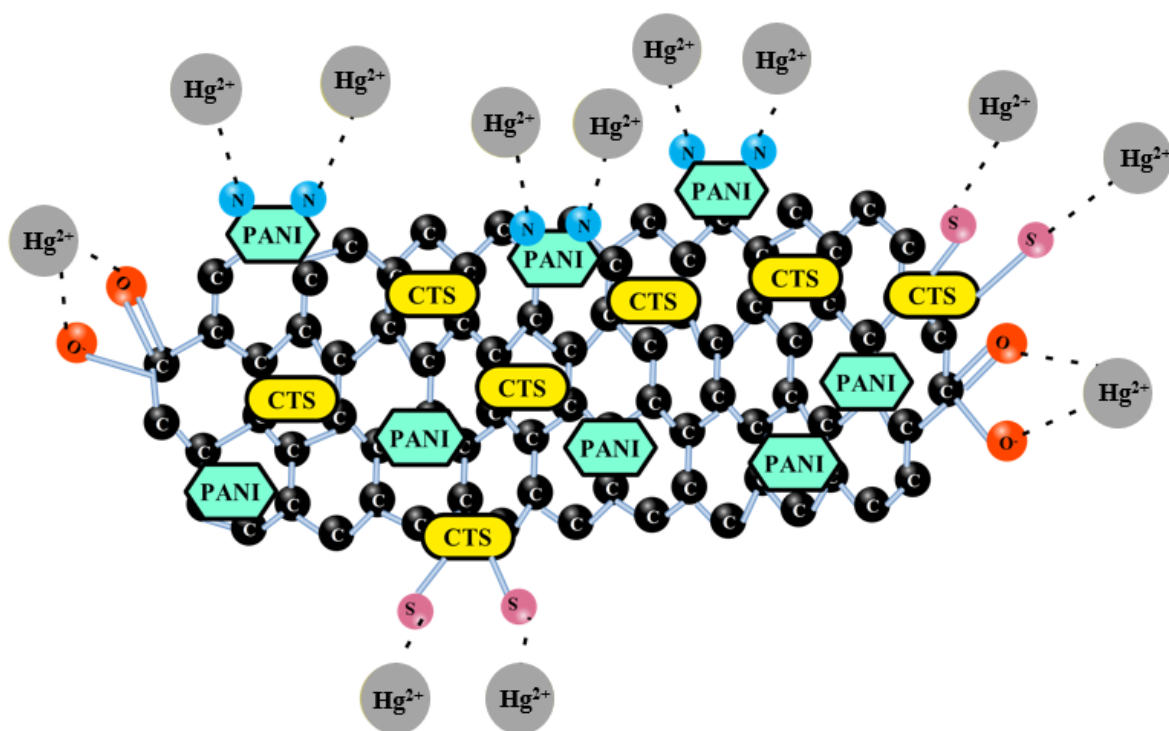
359

Figure 14. The contours of desirability fluctuations

360 **Adsorption mechanism**

361 **Figure 15** shows the mechanism of Hg^{2+} adsorption onto the GO-CTS-PANI adsorbent. The
362 figure shows that there are three main interactions between adsorbent and Hg^{2+} ions, which
363 include: (1)- electrostatic interaction between dissociated carboxylic acid groups of GO and
364 $HgOH^+$ ions (Awad et al., 2020) (2)- soft-soft interaction between Hg^{2+} and sulfur atoms of
365 CTS (Anirudhan et al., 2015; Gao et al., 2021; Santhana Krishna Kumar et al., 2013) and (3)-
366 chelating interaction between N and Hg^{2+} (Zeng et al., 2019).

367



368

369 **Figure 15. Adsorption mechanism of Hg^{2+} on to the GO-CTS-PANI**

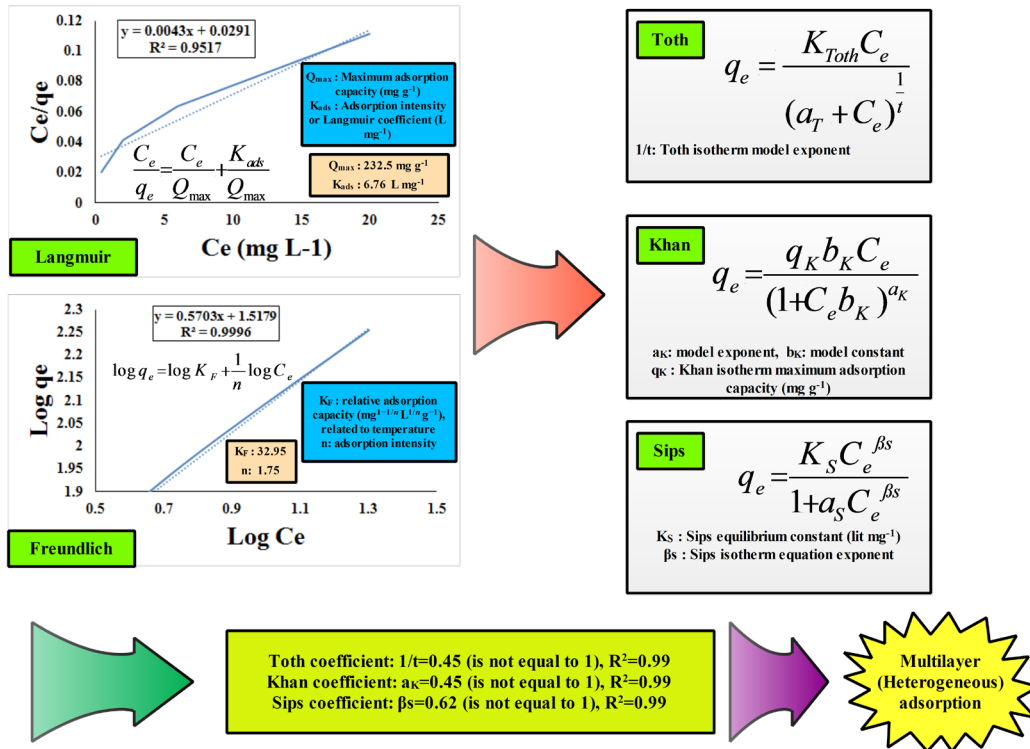
370

371 **Adsorption isotherm**

372 To evaluate the adsorption mechanism and determine the dominance of Freundlich and
373 Langmuir isotherms, two-parameter, and three-parameter equations (mentioned in **Figure 16**)
374 were applied. In the first step, two-parameter calculations are analysed as shown in **Figure 16**.

375 The outcomes indicate that the regression coefficient of both isotherms was over 0.95 and the
376 precise determination of the mechanism is simply not possible. Based on two-parameter
377 relationships, the maximum absorption capacity (Q_{max}), Langmuir coefficient (K_{ads}), K_f and n
378 were estimated as 232.5 mg g⁻¹, 6.76 L mg⁻¹, 32.95 and 1.75, respectively. However,
379 considering the three-parameter Sips, Khan and Toth isotherms (R^2 more than 0.99) and
380 modelling them in Curve Expert Professional software, it was revealed that the exponential
381 coefficients of the models did not converge to 1. Consequently, the Freundlich isotherm was
382 found to be superior (Eftekhari et al., 2020; Eftekhari et al., 2021). It was observed that Hg²⁺
383 ions were adsorbed onto GO-CTS-PANI in some sequential layers and $0 < 1/n < 1$ indicating a
384 favourable adsorption process. **Figure 17** shows that in Temkin model, $b < 8$ KJ mol⁻¹, and
385 according to the Dubinin-Radushkevich (D-R) equations, $E < 8$ KJ mol⁻¹. Therefore, the
386 adsorption of Hg²⁺ ions onto GO-CTS-PANI is physically in nature. The D-R isotherm model
387 was used to calculate the Q_m and K factors which were found to be 102 mg g⁻¹ and 2E-07,
388 correspondingly (Eftekhari et al., 2020).

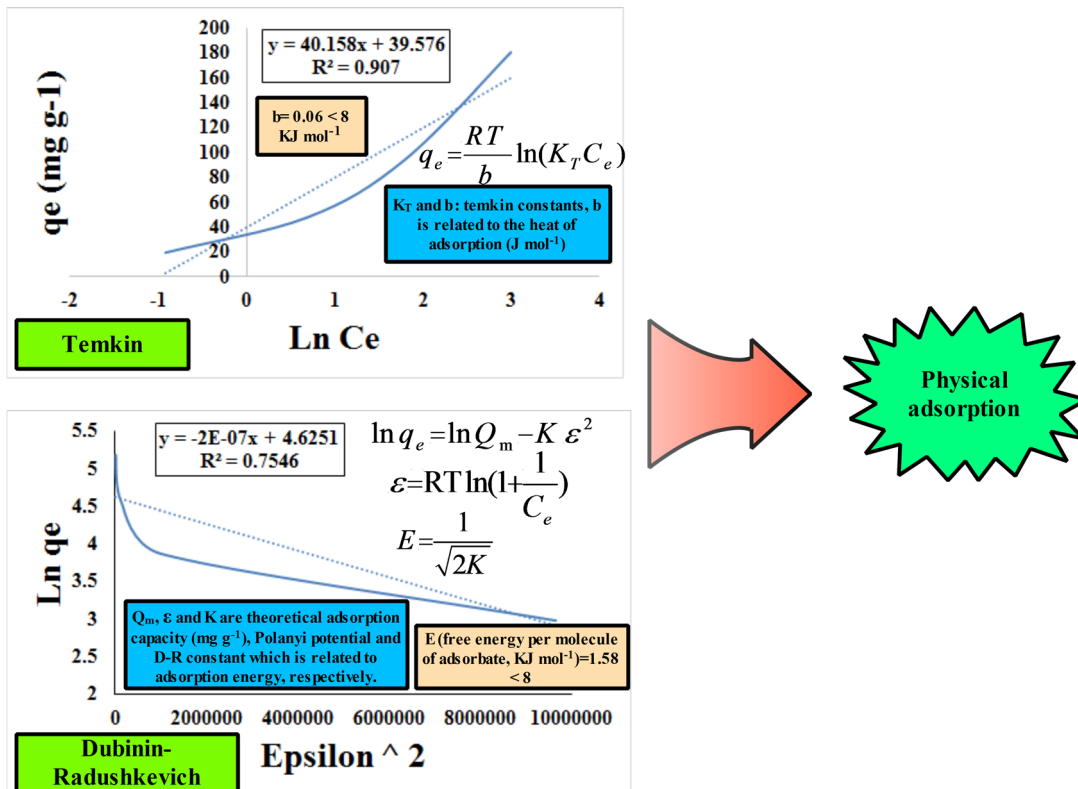
389



390

391

Figure 16. The computational model of Hg^{2+} adsorption onto GO-CTS-PANI.



392

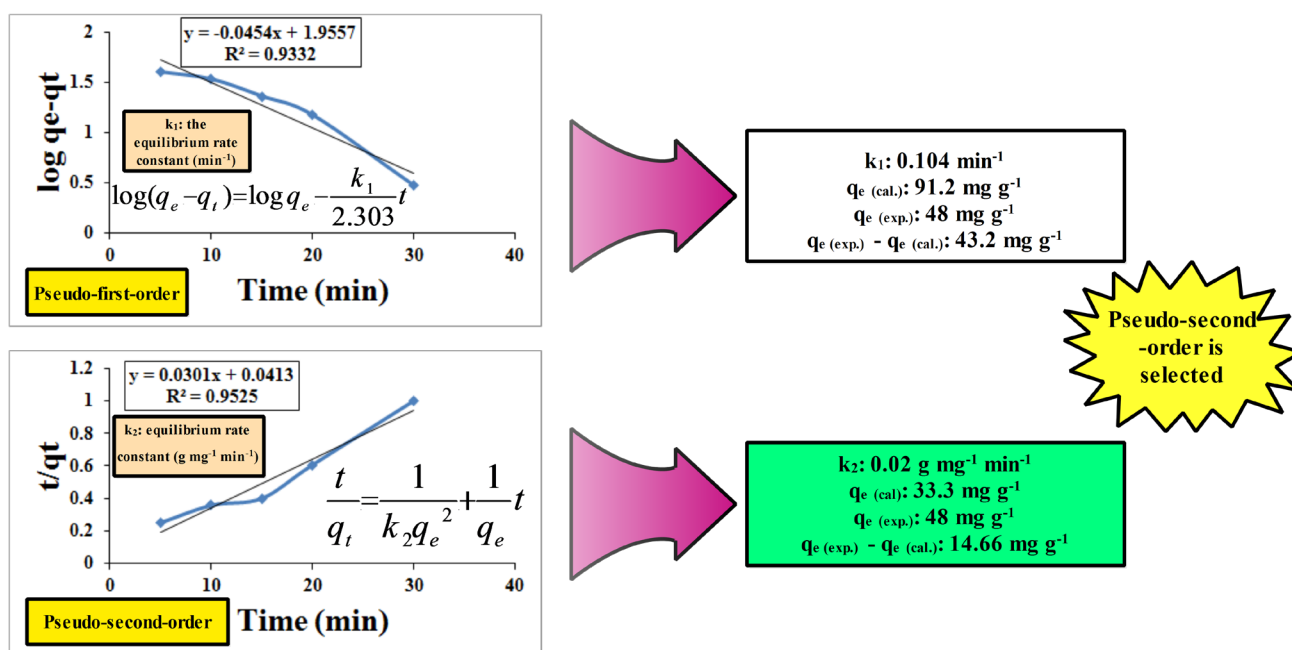
393

Figure 17. The physical, chemical, or intra-particle mechanism of Hg^{2+} adsorption onto GO-CTS-PANI.

394

395 **Adsorption kinetic**

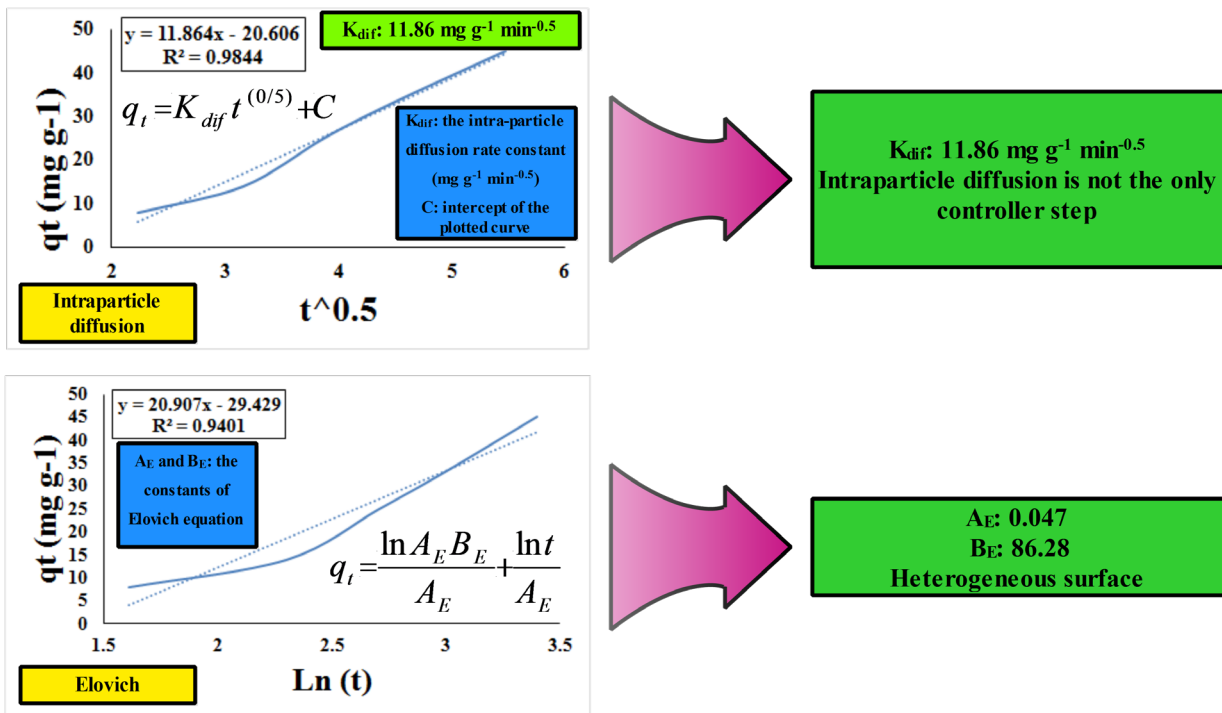
396 **Figures 18** and **19** demonstrate the results of Hg^{2+} kinetic adsorption onto GO-CTS-PANI
 397 using four models: Pseudo-First-Order (PFO), Pseudo-Second-Order (PSO), Intra-particle, and
 398 Elovich. Based on the data presented in **Figure 18**, the PSO model produced a more desirable
 399 R^2 value and a smaller difference between experimental and calculated q_e values compared to
 400 the PFO model. Therefore, it can be concluded that the adsorption of Hg^{2+} onto the GO-CTS-
 401 PANI follows by the pseudo second order model with a rate of $k_2=0.02 \text{ mg g}^{-1} \text{ min}^{-1}$ ($R^2=0.95$)
 402 (Eftekhari et al., 2020; Eftekhari et al., 2021).



406 **Figure 19** shows that it is evident that the kinetic behaviour of Hg^{2+} adsorption onto GO-CTS-
 407 PANI can be described by both Intra-particle ($R^2=0.98$) and Elovich ($R^2=0.94$) models. The
 408 Intra-particle kinetic curve has intercept of $C=-20.6$ indicating that both integrated intra-
 409 particle and mass transfer mechanisms play a significant role in the adsorption process

410 (Eftekhari et al., 2020). Moreover, the Elovich model suggests that GO-CTS-PANI has a
 411 heterogeneous surface which is consistent with the results of isothermal assessments.

412



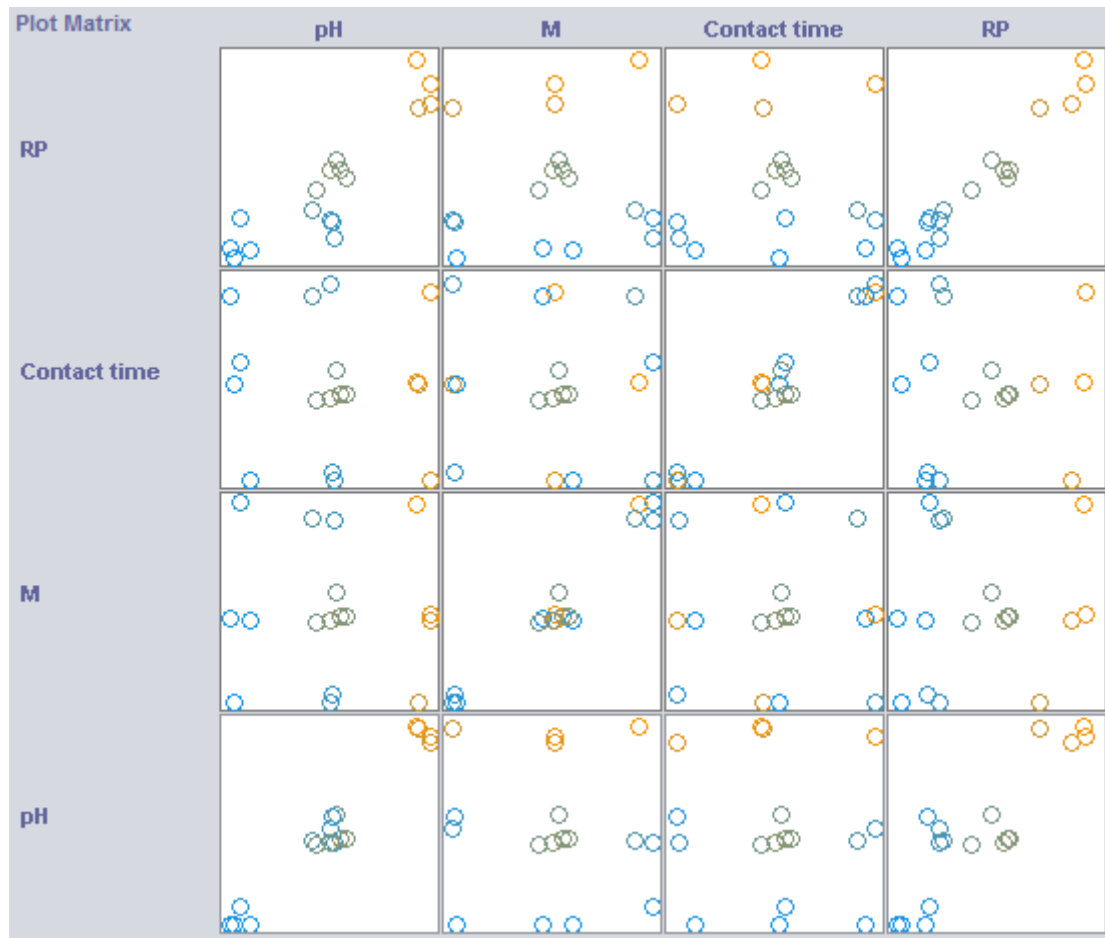
413

414 **Figure 19.** The outcomes of Elovich and Intra-particle kinetic models in the investigation.

415

416 **Machine learning**

417 This study also utilised machine learning practices for two purposes: (1) to improve the
 418 accuracy of prediction parameters and (2) to establish an intelligent infrastructure for online
 419 investigation of purification systems using the adsorption method. The distribution of data used
 420 in the machine learning process, carried out using the RF method is illustrated in **Figure 20.**



421

422

Figure 20. The distribution of data used for the machine learning modelling in this study.

423

424

425

426

427

428

429

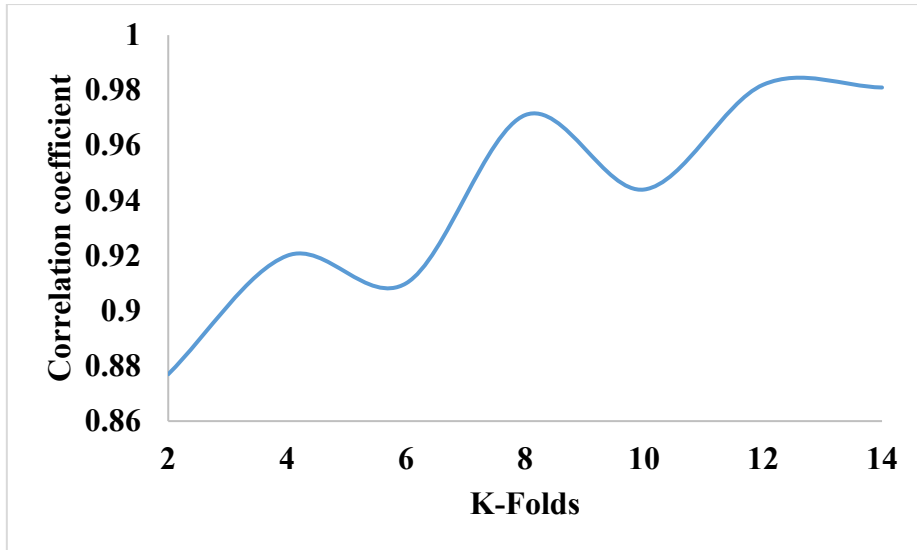
430

431

432

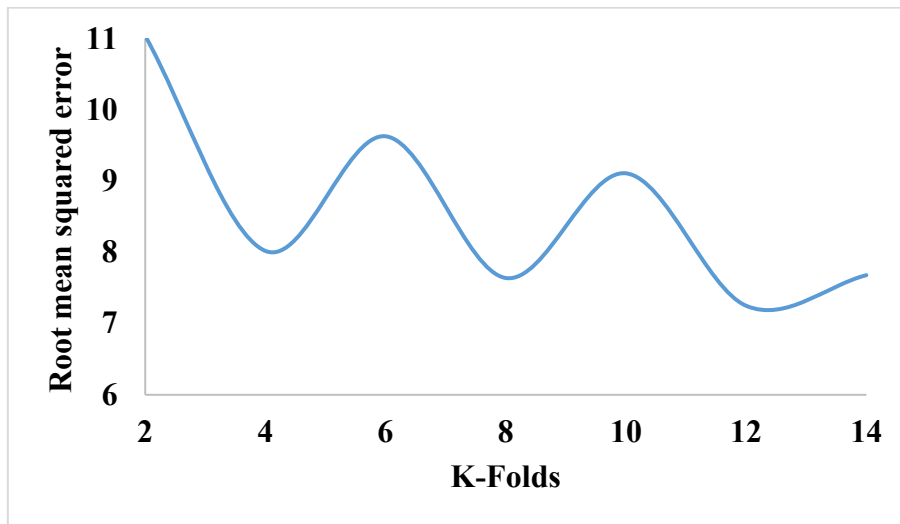
433

Figure 21 displays the performance of the RF algorithm at different K-Folds Cross-Validation (KFCV) during training and testing process of the data. By adjusting the number of folds, the proportion of testing and training data can be determined. The correlation coefficient (**Figure 21a**) and root mean square error (**Figure 21b**) both indicate that the correlation coefficient generally increases as the number of folds increases but with some fluctuations in different steps. conversely, the behaviour of root mean square error is similar to correlation coefficient but in reverse. Therefore, the best condition is achieved at K=12 and the details are summarised in Table 5. It is worth noting that by applying the RF algorithm, the prediction performance is improved, and operation of the adsorption process can be managed automatically without the need for further examinations or other mathematical computations.



434
435

(a)



436
437

(b)

438 **Figure 21. The effects of the number of K-folds on (a) correlation coefficient and (b) root mean square**

439

error

440

Table 5. The statistical indicators of the RF algorithm performance for K=12

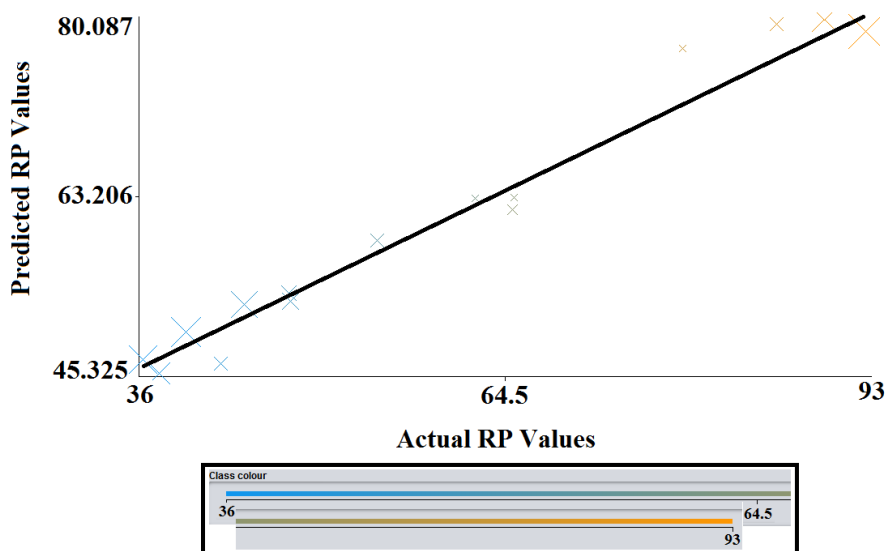
Correlation coefficient	98.2%
Mean absolute error	6.16
Root mean square error	7.25
RAE	38.7%
RRSE	38.26%
Total Number of Instances	17

441 **Figure 22** show the scatterplot between observed and predicted values of the removal
442 percentage (RP). It shows that the prediction process achieved high accuracy, providing
443 evidence of the high validity of the RF algorithm for optimising the adsorption of Hg^{2+} ions
444 onto GO-CTS-PANI nanocomposite. The development of a Decision Support Ssystem (DSS)
445 for the prediction of Hg^{2+} purification from water resources by adsorption process is an
446 important achievement, and the statistical outputs of the system are highly encouraging.

447 The system employs the RF algorithm and takes into account critical input variables, including
448 contact time, the quantity of adsorbent, and pH. The notably high correlation coefficient of
449 98.2% signifies a robust positive connection between the input variables and the outcome
450 variable, which, in this instance, pertains to the extent of Hg^{2+} removal. This strong correlation
451 coefficient indicates that the input variables possess substantial predictive power regarding the
452 outcome variable, a crucial characteristic of a dependable Decision Support System (DSS).
453 Mean Absolute Error (MAE) and Root Mean Square Error (RMSE) represent two common
454 metrics for gauging the accuracy of a prediction model. MAE reflects the average absolute
455 disparity between predicted and actual values, while RMSE signifies the square root of the
456 average squared difference between predicted and actual values. In this scenario, the MAE of
457 6.16 and the RMSE of 7.25 indicate that the DSS's predictions closely align with the actual
458 values. These low values underscore the high precision and reliability of the system's
459 predictions, a vital aspect for effective decision-making.

460 Furthermore, Relative Absolute Error (RAE) and Root Relative Square Error (RRSE) serve as
461 supplementary metrics for assessing prediction model accuracy. RAE quantifies the average
462 absolute discrepancy between predicted values and actual values, normalized by the average
463 actual value, while RRSE denotes the square root of the average squared difference between
464 predicted values and actual values, also normalized by the average actual value. In this context,
465 the RAE of 38.7% and the RRSE of 38.26% are relatively elevated. This implies that there

466 exists some degree of error in the DSS's predictions. Nevertheless, it is essential to note that
467 these values still fall within an acceptable range and do not diminish the overall reliability of
468 the system.



469

470 **Figure 22.** The scatter plot between predicted and actual values of RP% in RF algorithm (K=12)

471

472 **Test of Reusability**

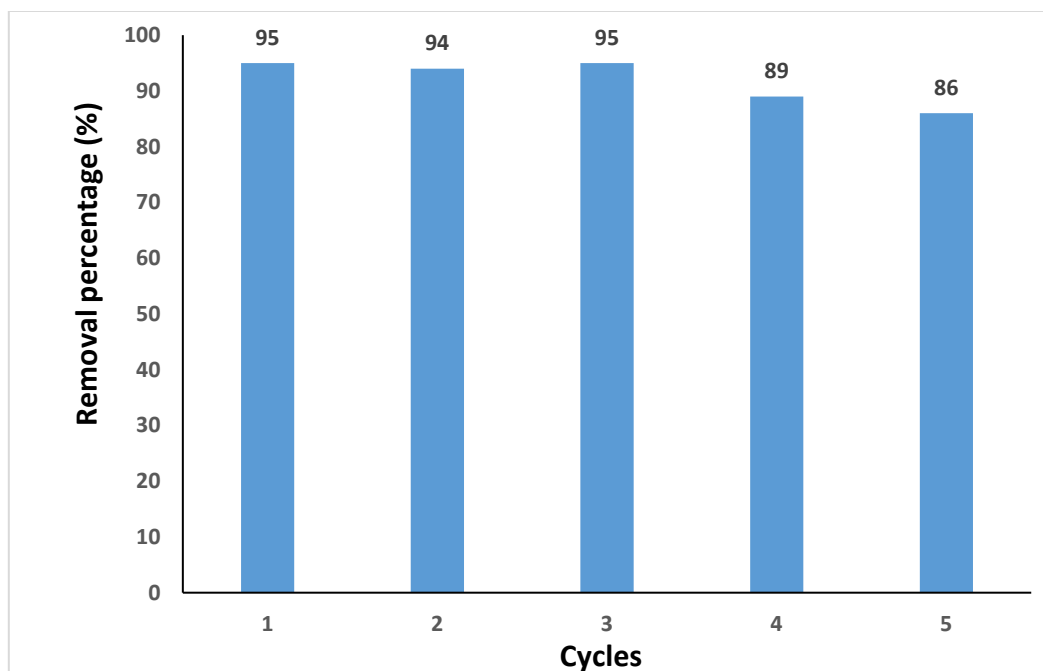
473 **To evaluate the potential for reusing GO-CTS-PANI, we conducted five cycles of adsorption**
474 **and desorption, employing a 0.1 mol L⁻¹ HCl (hydrochloric acid) solution for desorption.** As
475 depicted in **Figure 23**, following three rounds of utilizing the GO-CTS-PANI adsorbent, we
476 observed only a marginal 6% decrease in removal percentage (RP). Nevertheless, in subsequent
477 cycles, a more substantial reduction in RP became evident. Based on these observations, it can
478 be inferred that GO-CTS-PANI remains effective for up to three cycles without a noteworthy
479 decline in RP.

480

481

482

483



484

485 **Figure 23. Results of the reusability of GO-CTS-PANI nanocomposite**

486

487 **Comparison with other studies**

488 Table 6 provides a comparison between the newly developed GO-CTS-PANI composite in this
489 study and other adsorbents employed for Hg²⁺ removal. The findings clearly illustrate that this
490 novel adsorbent exhibits a remarkable adsorption capacity for Hg²⁺ within a short timeframe.
491 Furthermore, as it can be effectively reused for at least three cycles without a significant
492 reduction in removal percentage, the GO-CTS-PANI composite can be considered a highly
493 efficient adsorbent. According to the data in Table 6, it is evident that the GO-CTS-PANI
494 composite outperforms other adsorbents, such as palm shell activated carbon modified with
495 ionic liquids, in terms of adsorption capacity. This enhanced performance of the GO-CTS-
496 PANI composite can be attributed to its advantageous functional groups, including the sulfur
497 atoms found in CTS nanoplates, the presence of nitrogen atoms in PANI, and the electrostatic

498 interactions between the carboxylic acid groups of GO and Hg²⁺ ions. Consequently, these
 499 results strongly suggest that GO-CTS-PANI holds substantial promise as a material for
 500 effectively removing mercury from aqueous solutions.

501 **Table 6. Comparison between GO-CTS-PANI and other adsorbents for Hg²⁺ removal**

Adsorbent	Adsorption capacity (mg g ⁻¹)	Reference
2-mercaptobenzamide modified itaconic acid-grafted-magnetite nanocellulose composite	240.0	(Anirudhan and Shainy 2015)
Palm shell activated carbon impregnated with task-specific ionic-liquids	83.3	(Abu Ismaiel et al., 2013)
Polyamine modified reduced graphene oxide	63.8-59.9	(Yap et al., 2020)
Magnetic carbon nanotube	172.8	(Homayoon et al., 2017)
Mercapto-modified bentonite	19.3	(Sahan et al., 2018)
Mercaptobenzothiazole modified cellulose	204.1	(Krishna Kumar et al., 2013)
GO-CTS-PANI	232.5	This study

502

503 **Conclusions**

504 The GO-CTS-PANI composite proved effective as an adsorbent for eliminating Hg²⁺ from
 505 water samples. The optimal conditions, resulting in a 95% removal rate for 50 mg L⁻¹ Hg²⁺,
 506 were determined as follows: pH= 6.5, 12 mg of GO-CTS-PANI adsorbent, and a 30-minute
 507 contact period, employing the Box-Behnken method. The adsorption process exhibited a
 508 multilayer adsorption mechanism with physical interactions on the surface, as evident from
 509 conventional calculations. Kinetic analysis revealed that the adsorption reaction adhered to the
 510 PSO equation. Sensitivity analysis identified pH as the most influential factor impacting the
 511 adsorption process. Both RSM and machine learning techniques, specifically the RF method,
 512 proved effective for optimizing the adsorption process and predicting its efficiency,
 513 respectively. Furthermore, the GO-CTS-PANI nanocomposite demonstrated its reusability
 514 through five cycles of adsorption/desorption, with merely a 6% reduction in removal efficiency
 515 observed after three cycles. Ultimately, this study underscores the exceptional efficiency and

516 reusability of the GO-CTS-PANI composite as an adsorbent for Hg²⁺ removal, showcasing its
517 potential for future applications in water purification.

518

519 **References**

520 Abu Ismaiel A, Kheireddine Aroua M, Yusoff R (2013) Palm shell activated carbon
521 impregnated with task-specific ionic-liquids as a novel adsorbent for the removal of
522 mercury from contaminated water. *Chem Eng J* 225: 306-314.

523 Amini-Fazl MS, Barzegarzadeh M, Mohammadi R (2021) Surface Modification of Graphene
524 Oxide with Crosslinked Polymethacrylamide via RAFT Polymerization Strategy:
525 Effective Removal of Heavy Metals from Aqueous Solutions. *J Inorg Organomet Polym*
526 31: 2959–2970.

527 Albatrni H, Qiblawey H, El-Naas MH (2021) Comparative study between adsorption and
528 membrane technologies for the removal of mercury. *Sep Purif Technol* 257: 117833.

529 Anirudhan TS, Shainy F (2015) Effective removal of mercury(II) ions from chlor-alkali
530 industrial wastewater using 2-mercaptobenzamide modified itaconic acid-grafted-
531 magnetite nanocellulose composite. *J Colloid Interface Sci* 456: 22-31.

532 Arshad F, Selvaraj M, Zain J, Banat F, Abu Haija M (2019) Polyethylenimine modified
533 graphene oxide hydrogel composite as an efficient adsorbent for heavy metal ions. *Sep*
534 *Purif Technol* 209: 870-880.

535 **Awad FS, AbouZied KM, Abou El-Maaty WM, El-Wakil AM, Samy El-Shall M (2020)**
536 **Effective removal of mercury(II) from aqueous solutions by chemically modified graphene**
537 **oxide nanosheets. *Arab J Chem* 13: 2659-2670.**

538 Berg DM, Djemour R, Gütay L, Zoppi G, Siebentritt S, Dale PJ (2012) Thin film solar cells
539 based on the ternary compound Cu₂SnS₃. *Thin Solid Films* 520: 6291–6294.

540 Briffa J, Sinagra E, Blundell R (2020) Heavy metal pollution in the environment and their
541 toxicological effects on humans. *Heliyon* 6: e04691.

542 Eftekhari M, Akrami M, Gheibi M, Azizi-Toupkanloo H, Fathollahi-Fard AM, Tian G (2020)
543 Cadmium and copper heavy metal treatment from water resources by high performance
544 folic acid-graphene oxide nanocomposite adsorbent and evaluation of adsorptive
545 mechanism using computational intelligence, isotherm, kinetic, and thermodynamic
546 analyses. *Environ Sci Pollut Res* 27: 43999-44021.

547 Eftekhari M, Gheibi M, Azizi-Toupkanloo H, Hossein-Abadi Z, Khraisheh M, Fathollahi-Fard
548 AM, Tian G (2021) Statistical optimization, soft computing prediction, mechanistic and
549 empirical evaluation for fundamental appraisal of copper, lead and malachite green
550 adsorption. *J Ind Inf Integr* 23: 100219.

551 Gao P, Lei J, Tan J, Wang G, Liu H, Zhou L (2021) Self-assembled magnetic microcrystalline
552 cellulose/MoS₂/Fe₃O₄ composite for efficient adsorptive removal of mercury ions (Hg²⁺).
553 *Compos Commun* 25: 100736.

554 Ghadirimoghaddam D, Gheibi M, Eftekhari M (2023) Graphene oxide-cyanuric acid
555 nanocomposite as a novel adsorbent for highly efficient solid phase extraction of Pb²⁺
556 followed by electrothermal atomic absorption spectrometry; statistical, soft computing and
557 mechanistic efforts. *Inter J Environ Anal Chem* 103:469-490.

558 Global Mercury Assessment 2018. United Nation, Environmental Programme. **2019.**

559 Han Z, Guo Y, Yang W, Tang R, Wang H, Wu S (2020) Removal of mercury from flue gases
560 over iron modified activated carbon made by in situ ion exchange method. *J Energy Inst*
561 93: 1411-1418.

562 Homayoon F, Faghihian H, Torki F (2017) Application of a novel magnetic carbon nanotube
563 adsorbent for removal of mercury from aqueous solutions. *Environ Sci Pollut Res* 24:
564 11764–11778.

565 Jathar SB, Rondiya SR, Jadhav YA, Nilegave DS, Cross RW, et al., Ternary Cu₂SnS₃:
566 Synthesis, Structure, Photoelectrochemical Activity, and Heterojunction Band Offset and
567 Alignment. *Chem Mater* 33(6): 1983–1993.

568 Lei Y, Chen F, Luo Y, Zhang L (2014) Synthesis of three-dimensional graphene oxide foam
569 for the removal of heavy metal ions. *Chem Phys Lett* 593: 122-127.

570 Li L, Luo C, Li X, Duan H, Wang X (2014) Preparation of magnetic ionic
571 liquid/chitosan/graphene oxide composite and application for water treatment. *Int J Biol*
572 *Macromol* 66: 172-178.

573 Liu J, Duan Y, Song L, Zhang X (2018) Constructing sandwich-like polyaniline/graphene
574 oxide composites with tunable conjugation length toward enhanced microwave
575 absorption. *Org Electron* 63, 175-183.

576 Mbanga O, Ncube S, Tutu H, Chimuka L, Cukrowska E (2019) Mercury accumulation and
577 biotransportation in wetland biota affected by gold mining. *Environ Monit Assess* 191:
578 186.

579 Krishna Kumar AS, Kalidhasan S, Rajesh V, Rajesh N (2013) Adsorptive Demercuration by
580 Virtue of an Appealing Interaction Involving Biopolymer Cellulose and
581 Mercaptobenzothiazole. *Ind Eng Chem Res* 52: 11838–11849.

582 Raj D, Maiti SK (2019) Sources, toxicity, and remediation of mercury: an essence review.
583 Environ Monit Assess 191: 566.

584 Rezazadeh N, Danesh S, Eftekhari M, Farahmandzadeh M (2022a) Application of graphene
585 oxide and its derivatives on the adsorption of a cationic surfactant (interaction mechanism,
586 kinetic, isotherm curves and thermodynamic studies). J Mol Liq 368: 120720.

587 Rice KM, Walker EM, Wu M, Gillette C, Blough ER (2014) Environmental Mercury and Its
588 Toxic Effects. J Prev Med Public Health 47(2): 74–83.

589 Saadati T, Eftekhari M, Rezazadeh N, Nazarabad MK (2023) Graphene oxide–bismuth
590 tungstate (GO–Bi₂WO₆) nanocomposite as a green adsorbent for lead removal: isotherm,
591 kinetics and thermodynamic study. Int J Environ Sci Technol 20: 1301–1314.

592 Sahan T, Erol F, Yilmaz S (2018) Mercury(II) adsorption by a novel adsorbent mercapto-
593 modified bentonite using ICP-OES and use of response surface methodology for
594 optimization. Microchim J 138: 360-368.

595 Santana AJ, dos Santos WNL, Silva LOB, das Virgens CF (2016) Removal of mercury(II) ions
596 in aqueous solution using the peel biomass of *Pachira aquatica* Aubl: kinetics and
597 adsorption equilibrium studies. Environ Monit Assess 188: 293.

598 **Santhana Krishna Kumar A, Kalidhasan S, Rajesh V, Rajesh N (2013) Adsorptive**
599 **Demercuration by Virtue of an Appealing Interaction Involving Biopolymer Cellulose and**
600 **Mercaptobenzothiazole. Ind Eng Chem Res 52: 11838-11849.**

601 Shabani-Nooshabadi M, Zahedi F (2017) Electrochemical reduced graphene oxide-polyaniline
602 as effective nanocomposite film for high-performance supercapacitor applications.
603 Electrochim Acta 245: 575-586.

604 Streets DG, Devane MK, Lu Z, Bond TC, Sunderland EM, Jacob DJ (2011) All-Time Releases
605 of Mercury to the Atmosphere from Human Activities. *Environ Sci Technol* 45: 10485–
606 10491.

607 Tchounwou PB, Ayensu WK, Ninashvili N, Sutton D (2003) Environmental exposure to
608 mercury and its toxicopathologic implications for public health. *Environ Toxicol* 18(3):
609 149-75.

610 Vasudevan S, Lakshmi J, Sozhan G (2012) Optimization of electrocoagulation process for the
611 simultaneous removal of mercury, lead, and nickel from contaminated water. *Environ Sci*
612 *Pollut Res* 19: 2734–2744.

613 Velempini T, Pillay K (2019) Sulphur functionalized materials for Hg(II) adsorption: A review.
614 *J Environ Chem Eng* 7: 103350.

615 Wang C, Tian H, Jiang J, Zhou T, Zeng Q, He X, Huang P, Yao Y (2017) Facile Synthesis of
616 Different Morphologies of Cu₂SnS₃ for High-Performance Supercapacitors. *ACS Appl.*
617 *Mater. Interfaces* 9 (31): 26038–26044.

618 Wei Y, Zhang Y, Gao X, Ma Z, Wang X, Gao C (2018) Multilayered graphene oxide
619 membranes for water treatment: A review. *Carbon* 139: 964-981.

620 Yan X, Feng J, Li P, Li J, Ren B, Gao S, Cao R (2021) Fast and efficient removal of mercury
621 ions using zirconium-based metal–organic framework filter membranes. *Inorg Chem*
622 *Commun* 131: 108796.

623 Yap PL, Tung TT, Kabiri S, Matulick N, Tran DNH, Losic D (2020) Polyamine-modified
624 reduced graphene oxide: A new and cost-effective adsorbent for efficient removal of
625 mercury in waters. *Sep Purif Technol* 238: 116441.

626 Yu JG, Yue BY, Wu XW, Liu Q, Jiao FP, Jiang XY, Chen XQ (2016) Removal of mercury by
627 adsorption: a review. *Environ Sci Pollut Res* 23: 5056–5076.

628 Zaman MB, Poolla R (2020) Morphological tuning of hydrothermally derived visible light
629 active Cu₂SnS₃ nanostructures and their applications in photocatalytic degradation of
630 reactive industrial dyes. *Opt Mater* 104: 109853.

631 Zeng H, Wang L, Zhang D, Yan P, Nie J, Sharma VK, Wang C (2019) Highly efficient and
632 selective removal of mercury ions using hyperbranched polyethylenimine functionalized
633 carboxymethyl chitosan composite adsorbent. *Chem Engin J* 358: 253-263.

634

635

636

637

638

639

640

641

642

643

644

645

646

647

648

649 **Ethical approval**

650 Not applicable.

651 **Consent to participate**

652 Not applicable.

653 **Consent for publication**

654 Not applicable.

655 **Competing interests**

656 The authors declare no competing interests.

657 **Contributions**

658 Sara Enferadi: data curation, methodology; Mohammad Eftekhari: data curation, methodology,
659 supervision, conceptualization, writing—review and editing; Mohammad Gheibi:
660 methodology, software, writing—review and editing; Nikoo Nabizadeh Moghaddam: data
661 curation, methodology; Stanislaw Waclawek: writing—review and editing, and supervision;
662 Kouros Behzadian: data curation and conceptualization, supervision, writing—review and
663 editing.

664 **Funding**

665 There is no funding for this research.

666

667